Quantifying three-dimensional curvature of the nuclear lamina and the depletion of lamin B1

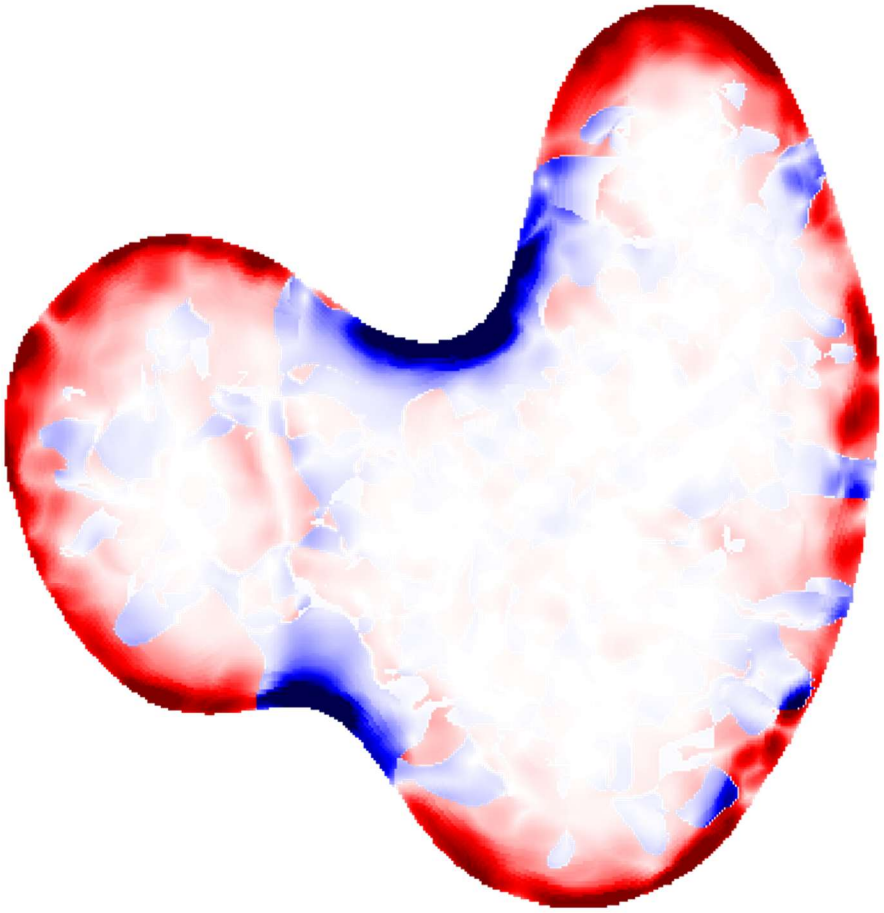

BSc thesis Nanobiology

W. W. T. van der Voort

Quantifying three-dimensional curvature of the nuclear lamina and the depletion of lamin B1

BSc thesis Nanobiology (NB3000)

by

Wouter W. T. van der Voort

5755344

Supervision:	Dr. Hylkje J. Geertsema
	Boyd C. Peters
Assessment committee:	Dr. Hylkje J. Geertsema
	Dr. Daan Brinks
Project duration:	February – June, 2025
Research group:	Geertsema Lab
	Department of Imaging Physics
	Delft University of Technology

ImPhys
Image to insight
Insight in imaging

TU Delft

Abstract

The nuclear lamina functions as a structural support system for the nucleus and must be broken down during mitosis. Not much is known about the process by which this breakdown is initiated. Prior studies have suggested that the nuclear envelope is depleted of lamin B1 at high curvatures, which destabilized the nuclear lamina and possibly plays a role in mitotic nuclear envelope breakdown. A statistical probability model has been proposed to describe this depletion based on the Gaussian curvature of the nuclear lamina. However, this model has only been tested on limited two-dimensional data. In this thesis, a quantitative image analysis pipeline is created and applied to test the relation between the absolute Gaussian curvature of the nuclear lamina and the density of lamin B1 in three-dimensional confocal images. To accomplish this, the nuclear lamina are segmented with unsharp-masking and steerable filters. The curvature of the nuclear lamina is computed using a grey-scale surface curvature estimation. Two different density states of the lamin B1 meshwork are found and a transition from high to low density is shown for increasing curvatures. These results support the previously proposed probability model for the depletion of lamin B1 at high curvatures and provides a deeper understanding of the structure of the nuclear lamina. Additionally, the image analysis pipeline established in this thesis provides helpful tools for effective segmentation and curvature estimation of the nuclear lamina and can be applied in future research.

Acknowledgements

Firstly, I would like to express my thanks to Dr. Hylkje Geertsema for welcoming me into the research group, for creating an open and accepting environment and for our encouraging weekly meetings. I am very grateful for the freedom that was given to me to explore the topics that interested me. I would also like to thank my daily supervisor Boyd Peters for supporting me during the entire thesis, for teaching me helpful coding skills and for always being available for any questions and challenges I encountered. I have fond memories of our collaboration, from fun conversations to insightful discussions. I would like to express my gratitude to Myron Hensgens for providing his data and images from the lab, for our nice daily talks in the office and for teaching me all the basics of the wet lab. Additionally, I would like to thank Aditya Mashkar for providing helpful feedback during our group meetings and all members of the Computational Imaging department for truly making me feel part of their research environment. I would also like to express my gratitude to Dr. Daan Brinks for taking the time to read my thesis report and being part of my examination committee. All these individuals have been vital to the success of this thesis, for which I am deeply grateful.

Contents

1 Introduction

1.1 The nuclear lamina

The nucleus of a cell contains a number of distinct structures, each with their own functions. One of these structures is the nuclear lamina. The nuclear lamina plays a variety of crucial roles in the cell, as shown in *figure 1*. One major function of the nuclear lamina is its interaction with chromatin. Lamina-associated domains (LADs) are genomic regions situated at the periphery of the nucleus, in close proximity to the nuclear lamina, and usually consist of dense and largely inactive heterochromatin [1], [2]. By regulating LADs and influencing chromatin structure, the nuclear lamina directly affects gene expression and has flow-on effects on gene regulation. Additionally, the nuclear lamina plays an important role in cellular mechanics through its interactions with the cytoskeleton. These interactions occur via membrane protein complexes such as the linker of nucleoskeleton and cytoskeleton (LINC-) complex [3], [4] and the nuclear pore complex (NPC) [5]. Post-translational modifications of the nuclear lamina are influenced by mechanical stress on the cell, showing the existence of mechanotransduction between the cytoskeleton and the nuclear lamina [6]. Disruptions to the structure or activity of the nuclear lamina can lead to a group of diseases known as laminopathies, including muscular dystrophy [7], lipodystrophy [8], leukodystrophy [9], neuropathy [10], and progeria [11].

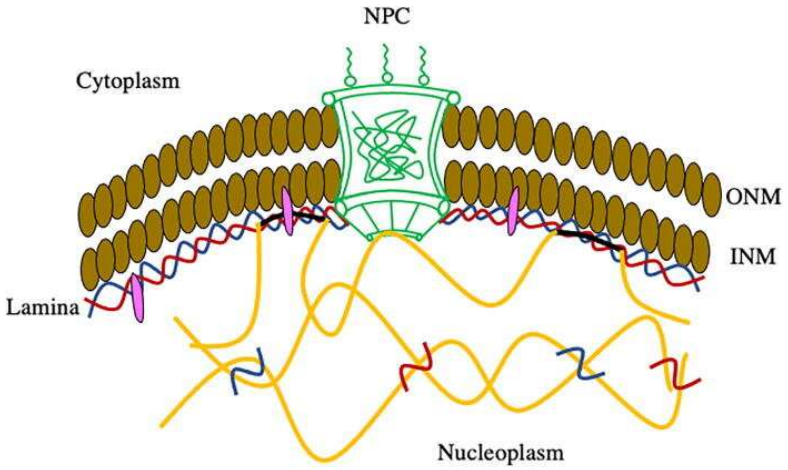

Figure 1. A schematic representation of a cross-section of the nuclear envelope. The nuclear envelope separates the cytoplasm and nucleoplasm with the outer nuclear membrane (ONM), the inner nuclear membrane (INM) and the nuclear lamina. The nuclear lamina consists of A-type and B-type lamins, depicted in red and blue, respectively. Lamins form separate but intertwined meshworks and interact with other nuclear components, such as lamina-associated proteins, depicted in pink, and the nuclear pore complex (NPC). Lamins also interact with lamina-associated domains (LADs), depicted in black, which usually are inactive regions of chromatin, depicted in yellow. Figure adapted from [12].

Importantly, the nuclear lamina forms a mechanical support structure for the nucleus, protecting chromatin from external forces. However, the structural integrity of the nuclear lamina poses a challenge during mitosis, as DNA must be released from the nuclear envelope before cell division can take place. In a process called nuclear envelope breakdown (NEBD), cytoplasmic kinases enter the nucleus and phosphorylate the nuclear lamina, leading to depolymerization and degradation of the nuclear lamina [13], [14]. The initiation of NEBD depends on the rupture of the nuclear envelope to allow kinase entry into the nucleus. How the rupture is formed and NEBD is initiated, remains largely unknown. A mitotic invagination of the nuclear envelope is regularly observed prior to NEBD and supports the belief that the initiation of NEBD is a mechanical process. This invagination forms close to the centrosomes and subsequently encapsulates them. The invagination is found to be dependent on the activity of microtubules and dynein [15], [16]. Several studies hypothesize the invagination to be a consequence of the centrosomes applying a tearing force on the nuclear envelope and thereby creating a distal rupture site, as shown in *figure 2*. Interestingly, it is also shown that rupture of the nuclear envelope depends on local curvature of the nuclear lamina [17]. The same results are found for experimentally induced curvature using micropipettes [17], [18], [19]. Additionally, nuclear structures with high curvature, such as micronuclei and blebs, show extreme depletion of the nuclear lamina [18]. It could therefore be hypothesized that the mitotic invagination is created to increase curvature of the nuclear envelope, thereby depleting the nuclear lamina and creating a rupture site to initiate NEBD. To further understand this process, a solid knowledge of the properties of the nuclear lamina is essential.

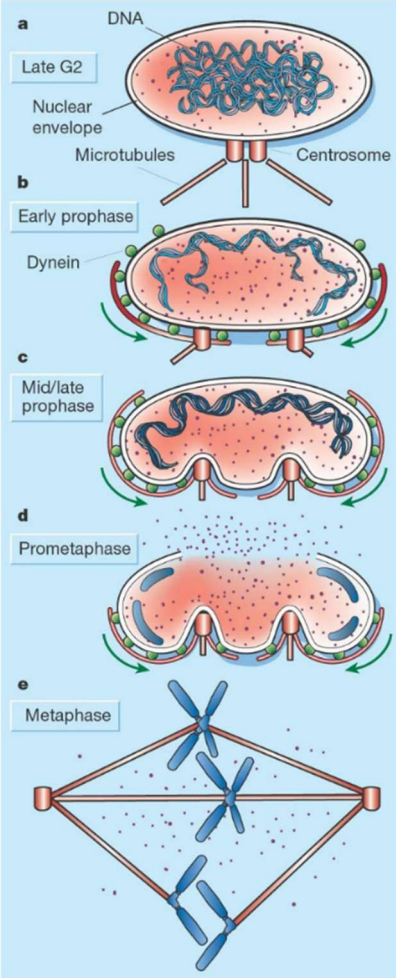

Figure 2. Stages of a proposed tearing mechanism to initiate nuclear envelope breakdown (NEBD) involving a mitotic invagination [15], [16]. **a.** In the late G2 phase of the cell cycle, the centrosomes position themselves alongside the nucleus. **b.** At initiation of mitosis, microtubules and dynein start pulling on the nuclear envelope. **c.** The tearing motion continues throughout the prophase, causing invaginations to occur around the centrosomes. **d.** During prometaphase, a rupture site is created and NEBD occurs. **e.** After NEBD, the mitotic process can resume. Figure obtained from [20].

1.2 Lamins and their properties

The nuclear lamina consists of a meshwork of lamin proteins along the inner surface of the nuclear envelope as shown in *figure 1*. Lamin proteins contain a long coiled-coil domain that enables monomers to associate into dimers, as shown in *figure 3a-b*. These dimers further polymerize into long filaments which are organized in an anti-parallel fashion, as illustrated in *figure 3c-d*. The individual filaments typically have a length of 380 nm and a width of 3.5 nm, and together they form a meshwork with a thickness of approximately 14 nm [21]. Different lamin types, or isoforms, are present in the nuclear lamina of mammalian cells. Two isoforms are classified as A-type lamins, namely lamin A and lamin C. In this thesis, the A-type lamins are referred to as lamin A/C. Lamin A/C is encoded by the *LMNA* gene and diverges by alternative splicing [22]. Additionally, there are two B-type lamins, namely lamin B1 and lamin B2. Lamin B1 and B2 are encoded by the *LMNB1* and *LMNB2* genes, respectively [23], [24]. All lamin isoforms are present in distinct but intertwined meshworks. The loss of one isoform has a great impact on the structure of the other lamin meshworks [25], [26]. Lamin A/C is present in a number of differentiated cells, while B-type lamins are present in many undifferentiated and differentiated cell types [27], [28]. Another critical difference between lamin A/C and B-type lamins is the farnesylation of the C-terminus of processed B-type lamins. This farnesyl group allows B-type lamins to directly interact with the lipid bilayer of the inner nuclear membrane (INM), as shown in *figure 1* [29]. The interaction between B-type lamins and the INM causes lamin A/C to be localized more to the center of the nucleus [17], [30].

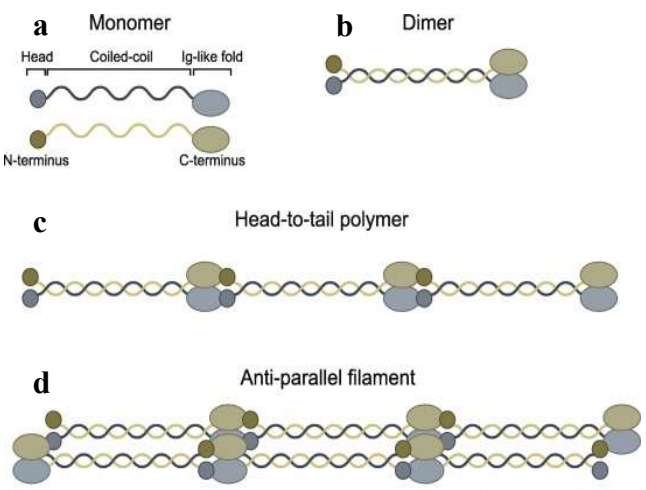

Figure 3. Formation of lamin filaments from lamin monomers. **a.** Lamin monomers consist of three domains: a head domain at the N-terminus, an Ig-like fold or tail domain at the C-terminus and a long coiled-coil domain in between. **b.** Dimers are formed by interactions between the coiled-coil domains of two lamin monomers. **c.** Single polymers are formed by head-tail interactions between lamin dimers. **d.** Lamin filaments are anti-parallel combinations of single polymers. Figure adapted from [31].

Understanding the mechanical properties of lamin filaments is essential to appreciate the role of the nuclear lamina in cellular processes. The persistence length, for which the filament can be considered to behave as a rigid rod, ranges from under 200 nm to 560 nm [21], [32]. The different lamin isoforms also exhibit distinct material properties. The ratio of A-type and B-type lamins in the nucleus correlates with nuclear stiffness [6]. A-type lamins are believed to behave like a viscoelastic fluid and impede deformations to the nucleus, while B-type lamins behave more like an elastic solid and restore nuclear deformations [33]. All lamin isoforms appear to be sensitive to the curvature of the nuclear envelope; however, the depletion of lamin A is additionally influenced by the strain rate of the curvature, likely due to its more fluid-like behavior [19]. In contrast, the depletion of B-type lamins does not show this viscoelastic time dependency.

1.3 Curvature of lamin B1

The purely elastic behavior, time-independent properties and relative rigidity of lamin B1 make it a suitable model for studying how curvature of the nuclear envelope affects the depletion of lamins during the initiation of NEBD. The depletion of lamin B1 and subsequent weakening of the nuclear lamina results in the rupture of the nuclear lamina as shown in *figure 4*. By observing these rupture sites, a probability model for the depletion of the lamin B1 meshwork at a given curvature of the nuclear lamina has been proposed [18]. The probability of lamin B1 presence at a specific curvature can be derived from this previously proposed model and is described in *formula 1*. This probability corresponds to the relative lamin density and local fluorescence intensity is used as a proxy for the local density of lamin B1.

$$P_{\text{lamin B1}} = (A - B)\,\frac{e^x}{1 + e^x} + B, x = \frac{E - a\sqrt{K}}{k_{\text{B}}T} - \frac{l_{\text{p}}\,L_{\text{fil}}\,K}{2} \quad (\mathbf{1})$$

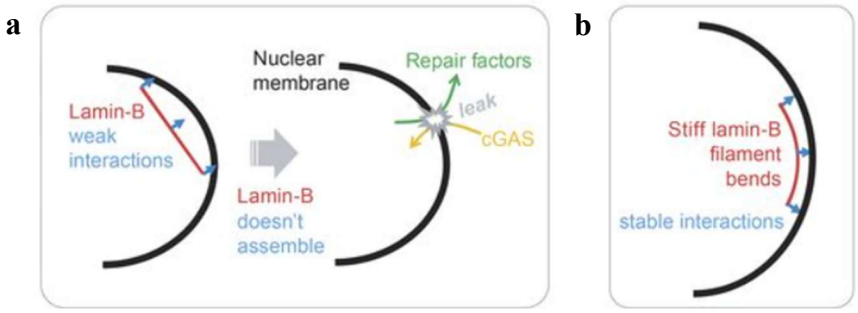

Figure 4. Proposed model for lamin B1 (here lamin-B) depletion at high curvatures. **a.** At high curvatures, lamin B1 only weakly interacts with the nuclear envelope, causing depletion of lamin filaments. In absence of lamin B1, the nuclear envelope is unstable and ruptures occur. **b.** At low curvature, lamin B1 strongly interacts with the nuclear envelope, creating a stable structure supporting the nuclear envelope. Figure adapted from [18].

The probability model described by *formula 1* relies on the Gaussian curvature K. Gaussian curvature represents the local amount of curvature of a surface, as shown *figure 5*, and is defined as the product of the two principal curvatures κ_1 and κ_2, as shown in *formula 2*. These principal curvatures are the inverse of the minimum and maximum radii of curvature, R_1 and R_2, respectively. The model is only valid for positive Gaussian curvature, as it depends on $\sqrt{K}$. The positive Gaussian curvature is the most relevant for the depletion of lamin B1 compared to other measures of curvature such as the mean curvature, because any filaments present on the curved surface must either conform to the positive Gaussian curvature or detach from the surface.

$$K = \kappa_1\,\kappa_2 = \frac{1}{R_1\,R_2} \quad (\mathbf{2})$$

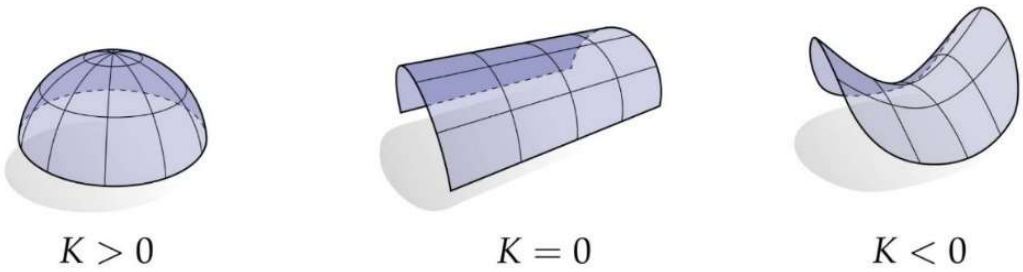

Figure 5. The Gaussian curvature K for three different surfaces. Gaussian curvature is the product of the two principal curvatures of a surface, resulting in a quantity for the local amount of curvature. Figure obtained from [34].

The probability model described by *formula 1* is based on the change of binding and bending energy for a single filament attached on a curved surface as shown in *figure 4*. The model uses the classical Boltzmann distribution and the partition function from statistical physics to describe the probability state for an entire system, resulting in a sigmoid probability function. The energy of a fully detached filament is set at zero, and the change of energy depends on several terms in the exponent. The first term in the exponent is the binding energy between the surface and the filament. Parameter E represents the binding energy over the full contact area between surface and filament. Parameter a represents the change in binding energy upon bending, which is subtracted from E. The ratio E/a determines the cut-off principal curvature κ_c and can be used to compute the midpoint of the sigmoid probability function. The binding energy term is normalized by the thermal energy $k_B T$. The second term in the exponent is the energy required to bend the filament. This bending energy depends on the persistence length l_p and filament length L_{fil} which together represent the stiffness of the filament. Lastly, A and B determine the upper and lower bound of the sigmoid probability function, respectively.

The density of lamin B1 appears to be relevant to the structural integrity of the nucleus and the initiation of NEBD [33]. Previous studies have examined the depletion and rupture of the lamin B1 meshwork due to high curvatures [17], [18], [19]. Despite promising models, most prior studies have been limited to two-dimensional images, discrete locations in the nuclear lamina, or artificially induced curvature. To our knowledge, no previous study has applied a three-dimensional quantitative analysis on endogenous curvature of the nuclear lamina and the distribution of lamin B1 across complete nuclei. **The aim of this thesis is to create and apply a quantitative image analysis pipeline to test the relation between the curvature of the nuclear lamina and the density of lamin B1 in three-dimensional images.** This is achieved by combining the theory from several prior studies [35], [36], [37] and applying it on confocal intensity data. The hypothesis is that two lamin B1 states with different intensities exist. The high-intensity state would represent an high-density lamin B1 meshwork and the low-intensity state would represent a low-density or depleted lamin B1 meshwork. The fraction of lamin B1 in the high-density state should decline for increasing curvature of the nuclear lamina following the sigmoid probability function described by *formula 1*.

2 Materials and methods

2.1 Sample preparation and data acquisition

All samples have been cultured, fixed and stained by Myron Hensgens and have been imaged at the Erasmus Medical Center. The samples are from the human ovarian cancer HeLa cell line which is often used as a model for cellular studies [38]. The cells were synchronized and fixed during mitosis with methanol. DNA was stained with DAPI and mmunostaining was used to target and visualize lamin A/C and lamin B1. This technique makes use of primary antibodies that bind to the protein of interest. Secondary antibodies with fluorophores are subsequently added to bind to the primary antibodies. The sample is then illuminated with an excitation laser to induce the emission of photons. For this study, lamin A/C and lamin B1 were stained with Alexa Fluor 488 (Alexa488) and Cysteine Dye 3 (Cy3), respectively. DAPI, Alexa488 and Cy3 were excited with lasers of wavelengths $\lambda = 355$ nm, $\lambda = 488$ nm and $\lambda = 561$ nm, respectively.

Samples were imaged with the Leica SP8 confocal microscope using a 63× Oil HC PL APO CS2 objective with numerical aperture (NA) 1.40. Confocal microscopes are similar to regular widefield microscopes, but add two confocal pinholes in the light path as shown in *figure 6*. These pinholes filter out the majority of out-of-focus light, which results in excellent optical sectioning. The emitted photons from the imaged section are redirected to the sensor by a beam splitter. Three-dimensional images of the samples were formed by stacking sections at different heights. Lastly, an important setting of the imaging procedure is the Nyquist rate, which is the maximum voxel size to obtain optimal resolution. For the used setup, the Nyquist rate was 0.050×0.050×0.149 µm. In practice however, the sampling rate can be approximately 40% larger to still achieve near-optimal resolution, resulting in a maximum voxel size of 0.070×0.070×0.209 µm.

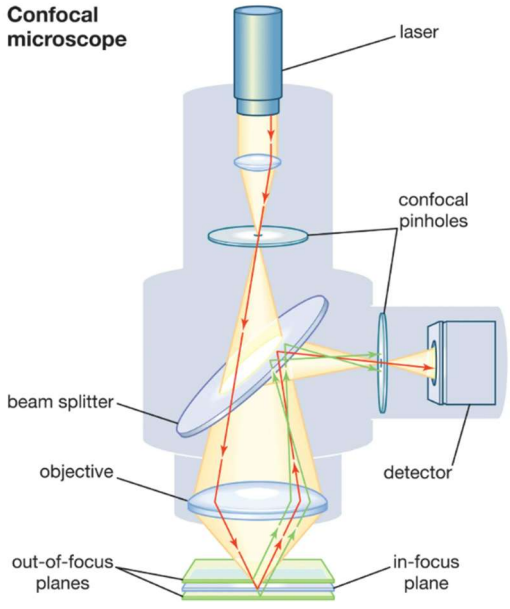

Figure 6. Schematic representation of a confocal microscope. Fluorophores in the sample are excited by a focused scanning laser and emitted photons are redirected to the detector by a beam splitter. Two confocal pinholes remove out-of-focus light, resulting in an image of a section of the sample. Figure obtained from [39].

2.2 Data analysis

The aim of this image analysis pipeline is to correlate the Gaussian curvature of the nuclear lamina with the intensity of lamin B1 signal. To achieve this, each field of view (FOV) was first made isotropic, followed by nucleus detection within each FOV. A rough segmentation of the nuclear lamina was created with unsharp-masking, after which a finer segmentation was accomplished with steerable filters. The three-dimensional curvature of the nuclear lamina was computed using an algorithm for grey-scale surface curvature estimation. The sign of the curvature was recovered from the isophote curvature of a representative solid object. For this study, the maximum signal of lamin A/C and lamin B1 was combined as a proxy for the nuclear lamina. The main goal of this proxy is to avoid the detection of holes in the nuclear lamina at locations where lamin B1 is not present. The principal curvatures of the nuclear lamina and the intensity of lamin B1 signal were recorded for the segmentation of the nuclear lamina, and the correlation between curvature and intensity was analyzed.

The pipeline was applied on a main dataset with confocal images of HeLa cell nuclei. The images were sampled close to the Nyquist rate mentioned in *section 2.1* with a voxel size of 0.061×0.061×0.180 μm. The main dataset contains fluorescence signal from DNA, lamin A/C and lamin B1. A supplementary dataset with voxel size 0.090×0.090×0.299 μm and fluorescence signal from lamin A/C and lamin B1 is presented in *appendix II*. Images were first converted to TIFF-files in FIJI [40] using the Bio-Formats package [41]. After this, Python was used throughout the full pipeline [42]. Python was selected over other platforms, such as FIJI, due to its ability to perform fast multi-dimensional computations, its high flexibility and its vast array of pre-existing packages and plugins. The packages that were used for this pipeline, are NumPy [43], scikit-image [44], SciPy [45] and Numba [46]. For illustrations and visualizations, the packages Matplotlib [47] and Napari [48] were used.

2.2.1 Image preparation

The provided images showed two asymmetrical or anisotropic properties. Firstly, the images had a different voxel size between the lateral and axial dimensions. The lateral voxel size – in the xy-plane – is determined by the pixel density of the camera sensor and the magnification of the microscope setup. The axial voxel size – in the z-direction – depends on the height difference between sequential sections that together form the three-dimensional image. Usually, the axial voxel size is larger than the lateral voxel size, making the voxels anisotropic. The second anisotropic property of the images was the blur of the fluorescence signal. This blur was caused by limitations inherent to the imaging equipment. Because light has a defined wavelength λ, there is a degree of uncertainty on the location of each fluorophore. On the image, this uncertainty is translated to a spread of intensity around the location of the fluorophore. The spread is characterized with the point spread function (PSF). The PSF is a three-dimensional function describing the intensity spread of a singular infinitesimally small emitter. The intensity profile of the PSF in any direction usually approximates a Gaussian function with a scale defined by its standard deviation σ. The PSF for confocal imaging is anisotropic between the lateral and axial profiles, with a wider profile in the axial direction as shown in *figure 7*.

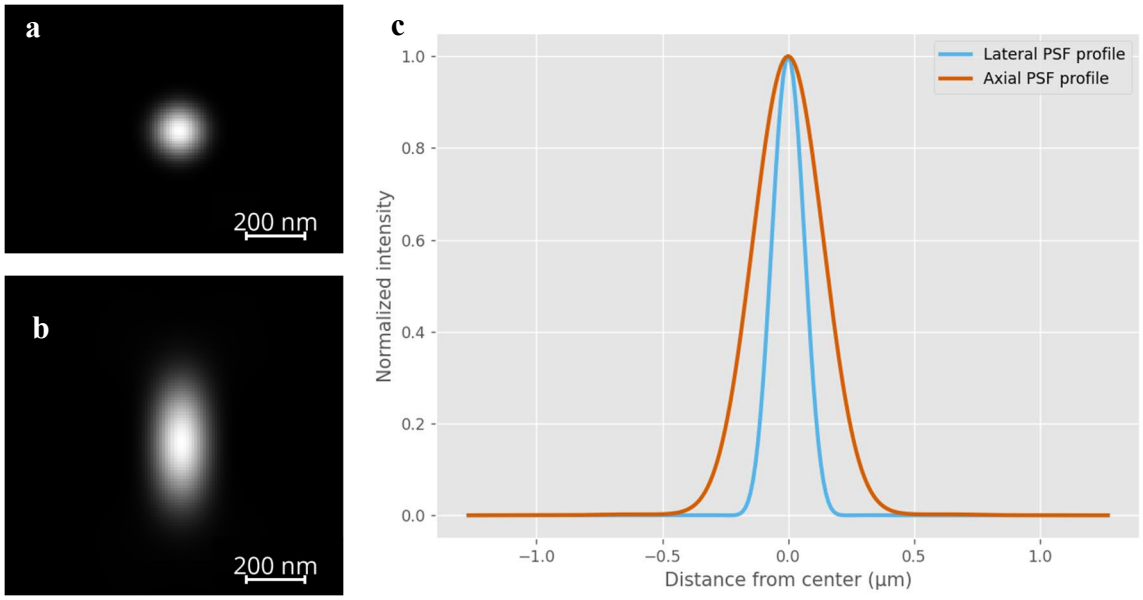

Figure 7. Shape of the point spread function (PSF) of the confocal microscopy setup used for this study. The PSF was computed for the largest used excitation wavelength λ_{max} = 561 nm, which results in the largest PSF for the nuclear lamina. **a.** Lateral cross-section of the PSF. **b.** Axial cross-section of the PSF. **c.** Lateral and axial intensity profiles of the PSF.

To make the voxel size isotropic, the axial voxel size was increased to match the lateral voxel size. The intensity values were interpolated to account for values of newly created voxels using spline interpolation. This method computes a smooth intensity function through all existing intensities by splitting the function up in shorter splines and fitting low-order polynomial functions on these intervals [49]. Spline interpolation with third order polynomials was applied for a smooth intensity function. Then, the axial voxel size was equalized to the lateral voxel size and the intensity values for the new voxels were derived from the computed interpolation function.

To overcome the anisotropy of the signal blur, additional Gaussian blurring was applied in the lateral dimensions to match the axial signal blur. Firstly, a Python implementation of the Gibson-Lanni model was used to simulate the PSF [50]. The Gibson-Lanni model approximates the PSF of an immersion objective microscope setup and accounts for light refraction in the sample, coverslip and medium [51]. A non-linear least squares regression curve fit was used to approximate the simulated PSF intensity profiles with Gaussian functions. This method uses an algorithm that adjusts the Gaussian parameters to optimize a fitted function on the simulated PSF intensity profile by minimizing by the squares of the residuals. The fitted standard deviations σ_{ax} and σ_{lat} approximate the scales of the axial and lateral PSF intensity profiles, respectively. The scale of the additional lateral blurring operation $\sigma_{lat,blur}$ was derived from the fact that variances – simply the squares of the standard deviations – of Gaussian functions are additive, as shown in *formula 3*. It is important to note that this blurring operation inherently reduces the lateral resolution of the image.

$$\sigma_{\mathrm{lat,blur}}{}^2 = \sigma_{\mathrm{ax}}{}^2 - \sigma_{\mathrm{lat}}{}^2 \quad (\mathbf{3})$$

After both the voxel size and the PSF are made isotropic, the images are ready for further analysis. The result of the full image preparation process on the nuclear lamina is shown in *figure 8*.

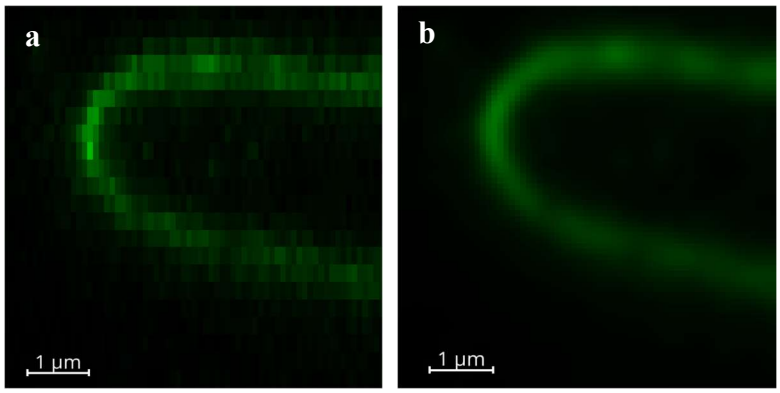

Figure 8. Lateral cross-section of the nuclear lamina, in this case the maximum of lamin A/C and lamin B1 signal, before and after the image preparation process. **a.** The nuclear lamina before image preparation, with anisotropic voxel size and signal blur. **b.** The nuclear lamina after image preparation, with isotropic voxel size and signal blur.

2.2.2 Labeling of valid nuclei

A single FOV may contain multiple nuclei. Since we are only interested in these nuclei, we first segmented the nuclei by their nuclear lamina to isolate relevant regions for analysis. Labeling nuclei by their nuclear lamina posed a challenge, because the nuclear lamina only forms a shell around the nucleus with low intensities across the inner portion of the nucleus. To address this issue, the axial maximum intensity projection (MIP) of the nuclear lamina, in this case the maximum of lamin A/C and lamin B1 signal, was used to detect nuclei in each FOV. The MIP produced a two-dimensional representation of the nuclei, which solved the aforementioned challenge posed by the hollow morphology of the nuclear lamina.

Nuclei in the MIP were segmented with an Otsu intensity threshold [52]. Otsu's method splits the intensity histogram of the MIP into two classes, which are considered to be the populations of background and foreground signal. The algorithm used for Otsu's method maximizes the inter-class variance – between the two classes – and minimizes the intra-class variance – within each class – to find the optimal threshold separating foreground and background signal. This technique is often used for thresholding problems in fluorescence microscopy, as it separates fluorescent signal from background noise relatively accurately. The resulting binary images contained small background artifacts. To remove these artifacts, all objects smaller than the typical size of a nucleus were removed, which for this dataset was determined to be 100 μm^2. It is important to note that this minimum size for a typical nucleus is highly dependent on both the cell type and the flatness of the nuclei in the sample.

A label was assigned to each nucleus to be able to perform the curvature analysis per nucleus. The nuclei in the two-dimensional binary image were labeled using the appropriate 2-connectivity approach as illustrated in *figure 9*. After all initial labels were assigned, the labels adjacent to the edge of the image were recorded to be removed later in the process. Subsequently, all labels were expanded over a distance indicated by the user-defined parameter *d*. Any pixels within the expansion range of multiple labels were assigned to the label closest to that pixel. After this expansion was completed, the previously recorded edge-adjacent labels were removed. This order of actions is important for two reasons. Firstly, edge-adjacent labels must be expanded to constrain the expansion of neighboring labels. Secondly, recording the edge-adjacent labels after expansion is completed, would result in the unnecessary removal of additional nuclei close to the edge.

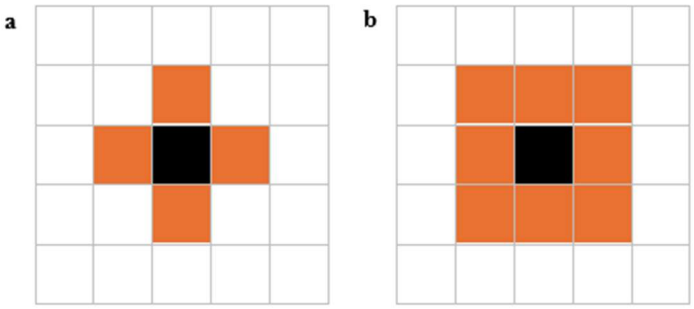

Figure 9. Two different types of connectivity for labeling pixels in an image. The pixel to be labeled is depicted in black and the pixels checked for existing labels are depicted in orange. **a.** 1-connectivity combines pixels that are horizontally or vertically connected. **b.** 2-connectivity combines pixels that are horizontally, vertically or diagonally connected.

Finally, the labels were applied to the three-dimensional isotropic images by projecting the two-dimensional labels in the axial dimension. To isolate each nucleus for analysis, the intensity values outside the label were set to 0. The remaining intensities of the nucleus were normalized per nucleus. This individual normalization is important to compensate for fluorescence intensity differences between different nuclei and different FOVs. The result of labeling valid nuclei in a typical dataset is shown in *figure 10*.

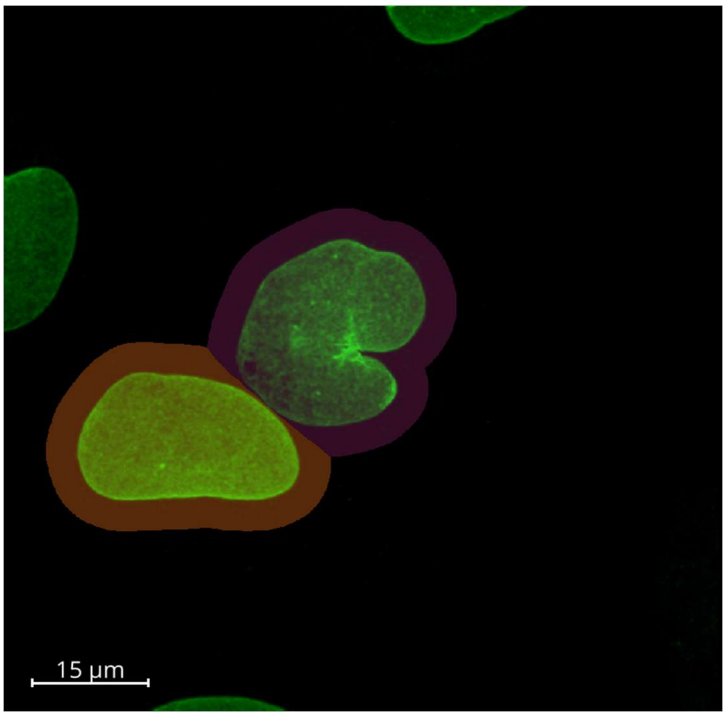

Figure 10. Labeling of valid nuclei for a typical dataset. The nuclear lamina, in this case a combination of lamin A/C and lamin B1, is depicted in green, and two separate labels are depicted in opaque orange and purple. Neighboring nuclei are separated properly and edge-adjacent nuclei are not labeled.

2.2.3 Segmenting the nuclear lamina

2.2.3.1 Rough segmentation

The nuclear lamina were segmented, since we are only interested in its local curvature and intensity. However, creating a continuous mask for a relatively non-uniform hollow object such as the nuclear lamina posed a significant challenge. For this analysis, a method called unsharp-masking was used [36]. This technique emphasizes local contrasts and detects edges of a three-dimensional non-uniform object. The first step was to compute a Gaussian blurred version I_b of the nuclear lamina, in this case the maximum of lamin A/C and lamin B1 signal. The scale σ_m of this blurring operation is a critical parameter for the segmentation method. The image I_b was multiplied and shifted by parameters α and β, respectively, to obtain the threshold image I_t as described in *formula 4* and shown in *figure 11*. Here, parameter α is a compression factor for the dynamic range of I_b and β is a minor positive shift to compensate for this compression. Together, these parameters determine how much contrast is retained in I_t.

$$\boldsymbol{I}_t = \alpha\, \boldsymbol{I}_b + \beta \quad (\mathbf{4})$$

A third parameter, denoted as i_c, can be deduced from these two parameters by *formula 5*. It is conventional to set the parameters α and i_c and subsequently deduce β from these values, as the former two have a more direct interpretation for the segmentation process. The parameter α is interpreted as the measure of accuracy of I_t compared to the isotropic image of the nuclear lamina. The parameter i_c is the cut-off intensity, at which the edges of the mask will be defined. The parameter i_c is usually denoted as a fraction of the global maximum intensity of I_b.

$$i_c = \frac{\beta}{1-\alpha} \quad (\mathbf{5})$$

The image I_t was subtracted from the original isotropic image, resulting in the unsharp-masking image as shown in *figure 11*. A zero-threshold was applied on the unsharp-masking image to obtain a binary mask. For each labeled nucleus, only the largest component of the mask was kept, resulting in a single mask per nucleus. This mask is referred to as the rough segmentation.

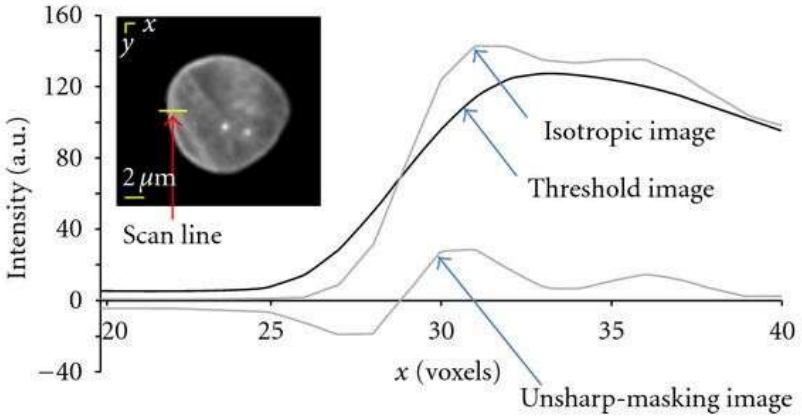

Figure 11. Local intensity profiles of three images relevant for the segmentation process of the nuclear lamina with the unsharp-masking method. The isotropic image, the threshold image (I_t) and the unsharp-masking image are compared. To obtain the rough segmentation of the nuclear lamina, a zero-threshold was applied on the unsharp-masking image. Figure adapted from [36].

2.2.3.2 Fine segmentation

The rough segmentation includes many low-intensity voxels for each 'true' voxel of the nuclear lamina, which obscure the correlation between curvature and intensity. The mask by rough segmentation has a width of several voxels and thus covers many voxels that do not cover the nuclear lamina as shown in *figure 12*, since the thickness of the nuclear lamina is only approximately 14 nm [21]. A thinner mask was needed to only include the voxels that cover the nuclear lamina.

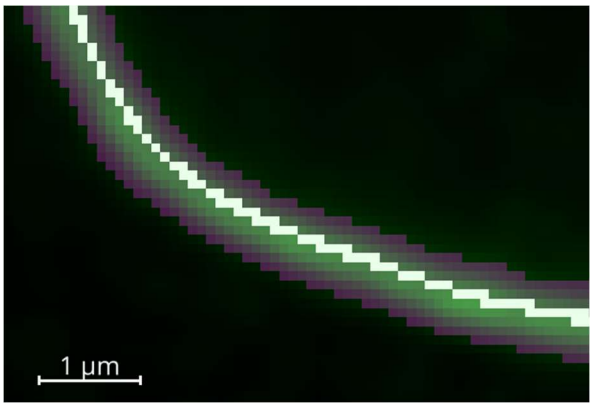

Figure 12. Cross-section of masks by rough segmentation, depicted in opaque magenta, and fine segmentation, depicted in white, for the nuclear lamina, depicted in green. Many low-intensity voxels around the maximum intensity ridge are included in the mask by rough segmentation for each 'true' voxel at the maximum intensity ridge. The mask by fine segmentation is localized to the maximum intensity ridge of the nuclear lamina.

To create a thinner mask for the nuclear lamina, a steerable filter for surface detection was used on the nuclear lamina, in this case the maximum of lamin A/C and lamin B1 signal [53]. Non-maximum suppression (NMS) and thresholding were applied on this filtered image. A Python implementation for this approach was present in the lab's repository. Steerable filters are linear combinations of basic filter kernels, as shown in *figure 13*, and can be used to find local response and orientation of specific structures, such as curves and surfaces in three-dimensional images [53], [54]. The scale of this kernel is specified by the parameter σ_s. The response and optimal orientation of the kernel, which represents the normal vector of the detected surface, were recorded for each voxel. NMS was applied on the response and orientation values. This method selects the maximum response voxel in the direction of the normal vector. Subsequently, a zero-threshold was applied on the NMS image, resulting in a binary image representing all surfaces detected in the isotropic image. The intersection of the masks by rough and fine segmentation was computed and the largest component of this combination was retained. This method resulted in a narrow surface-like mask localized on the maximum intensity ridge of the nuclear lamina. This new mask is referred to as the fine segmentation.

a **b**

Figure 13. Two types of three-dimensional steerable filter kernels for detection of image structures. Positive kernel factors are depicted in black and negative kernel factors are depicted in grey. **a.** The kernel for curve detection. **b.** The kernel for surface detection. Figure adapted from [53].

2.2.4 Computation of curvature

A method for surface curvature estimation in three-dimensional grey-scale images was used [35]. Firstly, the blurred gradient structure tensor (GST) was calculated for the nuclear lamina, in this case the maximum of lamin A/C and lamin B1 signal. The GST field of an *n*-dimensional image is the outer product of its gradient vector field $\vec{\nabla} I$ as shown in *formula 6* and results in a tensor field with $n \times n$ matrices. Each matrix element represents the product of two first-order partial derivatives $\boldsymbol{I}_{x,y,z}$. Two parameters are relevant for the calculation of the blurred GST field. Firstly, the parameter σ_g represents the scale of the Gaussian derivative function for the gradient vector elements. Secondly, the parameter σ_t represents the scale of the Gaussian kernel that is used to blur the individual GST elements over all three dimensions of the image. Once the blurred GST field was calculated, the eigenvectors and corresponding eigenvalues were computed for each GST matrix in the tensor field. For this thesis, a fast and accurate Python algorithm from the lab's repository was used. The resulting eigenvectors were sorted by the magnitude of their respective eigenvalues. The highest eigenvalue for each GST matrix corresponds to the eigenvector representing the normal vector $\vec{v}_n$, which is perpendicular to the local surface. The two remaining eigenvalues correspond to the eigenvectors representing the two principal directions of the surface $\vec{v}_1$ and $\vec{v}_2$, which are parallel to the local surface, perpendicular to each other and contain the principal curvatures κ_1 and κ_2, respectively.

$$\mathrm{GST} = \begin{pmatrix} \boldsymbol{I}_x \boldsymbol{I}_x & \boldsymbol{I}_x \boldsymbol{I}_y & \boldsymbol{I}_x \boldsymbol{I}_z \\ \boldsymbol{I}_y \boldsymbol{I}_x & \boldsymbol{I}_y \boldsymbol{I}_y & \boldsymbol{I}_y \boldsymbol{I}_z \\ \boldsymbol{I}_z \boldsymbol{I}_x & \boldsymbol{I}_z \boldsymbol{I}_y & \boldsymbol{I}_z \boldsymbol{I}_z \end{pmatrix} = \vec{\nabla} \boldsymbol{I} \otimes \vec{\nabla} \boldsymbol{I} \quad (\mathbf{6})$$

Usually, the principal curvatures can be computed by taking the magnitude of the derivative of the normal vector in the principal directions. However, Knutsson mapping was applied to the normal vector field before the principal curvatures were computed [55]. An implementation of Knutsson mapping is present in the MATLAB environment DIPimage [56], of which a Python implementation was used. Knutsson mapping takes the outer product of the normal vectors and divides it by the magnitude of the normal vector to generate a tensor field from a vector field, as shown in *formula 7*. This step was required, as the nuclear lamina is a hollow shell and not a solid object. The normal vectors on both sides of the shell have opposing directions, implying a discontinuity in the derivatives of the normal vector field along the maximum intensity ridge of the shell. Applying Knutsson mapping on the normal vectors lifts this discontinuity.

$$\boldsymbol{M} = \frac{\vec{v}_n \otimes \vec{v}_n}{\|\vec{v}_n\|} \quad (\mathbf{7})$$

The magnitudes of the directional derivatives of the tensor field in the principal directions are proportional to the absolute principal curvatures $|\kappa_1|$ and $|\kappa_2|$, as shown in *formula 8*. A Gaussian derivative function was used with scale parameter σ_t. The magnitude of the derivative tensor field is proportional to the principal curvatures by a factor of $\sqrt{2}$ caused by the uniform stretch property of Knutsson mapping. The product of the absolute principal curvatures $|\kappa_1|$ and $|\kappa_2|$ represents the absolute Gaussian curvature $|K|$ as described by *formula 2*. The sign of the principal curvatures was lost during the computation, but can be recovered afterwards in the case of a closed grey-scale shell as described in *section 2.2.5*.

$$|\kappa_{1,2}| = \frac{1}{\sqrt{2}} \left\| \vec{\nabla}_{\vec{v}_{1,2}} \boldsymbol{M} \right\| \quad (\mathbf{8})$$

The computation of absolute principal curvatures has a limit, which is determined by the resolution of the image. Specifically, the principal curvature cannot be reliably computed when a radius of curvature $R_{1,2}$ is smaller than the radius of the PSF of the image. The lower limit for the radii of curvature $R_{\min}$ and the upper limit for the absolute principal curvature $|\kappa_{\max}|$ were calculated from the NA and maximum excitation wavelength $\lambda_{\max}$ of the microscopy setup with *formula 9*, using the approximation that PSF radius is half of initial axial PSF extend. Despite the use of axial PSF extend, the calculated limit is valid for all three dimensions as the PSF of the image was made isotropic as described in *section 2.2.1*.

$$\frac{1}{|\kappa_{\max}|} = R_{\min} = \frac{2\,\lambda_{\max}}{\mathrm{NA}^2} \quad (\mathbf{9})$$

The curvature limit also implies that the scale σ_h of the combined blurring operations for curvature computation should be smaller than $R_{\min}$, to prevent these operations from influencing the computed curvature values too much. The curvature scale σ_h can be calculated as described in *formula 10* by using the variance addition rule from *formula 3*.

$$\sigma_h{}^2 = \sigma_g{}^2 + \sigma_t{}^2 + \sigma_k{}^2 \quad (\mathbf{10})$$

2.2.5 Sign recovery for principal curvatures

A solid representation of the nucleus is required to recover the sign for the principal curvatures. To this end, we used DAPI signal from DNA inside the nucleus. A thresholding operation was applied on the three-dimensional DAPI image using Otsu's method as described in *section 2.2.2*. Holes in the binary image were closed and only the largest component of each nucleus was retained. The resulting binary image was blurred with a Gaussian kernel defined by the curvature scale σ_h computed previously by *formula 10*, as this is also the blurring scale of the previously computed curvature.

The sign recovery for principal curvatures is based on the isophote curvature [35], [37]. First, the Hessian matrix $\boldsymbol{H}$ was computed for each voxel of the image. The Hessian is similar to the GST, but differs by applying the cross product on the gradient vector $\vec{\nabla}$ before using the derivative operation on the image $\boldsymbol{I}$, as shown in *formula 11*. The scale of the Gaussian derivative function is defined by σ_h as previously calculated with *formula 10*. For any *n*-dimensional image, the Hessian field results in a tensor field of $n \times n$ matrices. Each matrix element represents a second-order partial derivative $\boldsymbol{I}_{xx,xy,\ldots}$.

$$\boldsymbol{H} = \begin{pmatrix} \boldsymbol{I}_{xx} & \boldsymbol{I}_{xy} & \boldsymbol{I}_{xz} \\ \boldsymbol{I}_{yx} & \boldsymbol{I}_{yy} & \boldsymbol{I}_{yz} \\ \boldsymbol{I}_{zx} & \boldsymbol{I}_{zy} & \boldsymbol{I}_{zz} \end{pmatrix} = (\vec{\nabla} \otimes \vec{\nabla})\, \boldsymbol{I} \quad (\mathbf{11})$$

To compute the principal isophote curvatures, the Hessian was rotated to align with the principal directions of the object surface. Then, the the directional derivatives in the principal directions were extracted from the Hessian and their two eigenvalues were computed. A simple way to calculate these eigenvalues was to compute the quadratic forms Q_1 and Q_2 of the Hessian for each principal direction vector $\vec{v}_1$ and $\vec{v}_2$, respectively, as shown in *formula 12*. These quadratic forms are the principal isophote curvatures of the solid object.

$$Q_{1,2} = \vec{v}_{1,2}{}^{\mathrm{T}}\, \boldsymbol{H}\, \vec{v}_{1,2} \quad (\mathbf{12})$$

The correct sign of the principal curvature is the opposite of the isophote solution, because of intrinsic properties of the second derivative of a curve. For any convex structure such as the outside of a spherical nucleus, the second-order derivative will be negative, while the principal curvature should be positive. Likewise, the second-order derivative of a concave surface will be positive while the principal curvature should be negative. Because of this paradox, the opposite sign is applied to the principal curvatures κ_1 and κ_2 obtained in *section 2.2.4*, thereby recovering the sign of the principal and Gaussian curvatures.

It was decided not to apply sign recovery for the principal curvatures in the main result analysis, and the absolute Gaussian curvature was used instead. This decision was based on the low quality of sign recovery for the main dataset. A supplementary analysis including sign recovery is presented in *appendix I*.

2.2.6 Finding robust parameters

Parameter values for a number of steps in the image analysis pipeline had to be determined. These parameters were tuned to make the results more robust and stable for the main dataset. A robust value for any parameter depends on image properties such as voxel size, signal blur, object size, signal intensity and signal-to-noise ratio. Additionally, some parameter values were inherently limited. The segmentation parameter α is a compression factor between 0 and 1 [36], the cut-off intensity i_c is a fraction of the maximum intensity of $\boldsymbol{I}_b$ [36], the blurring scales σ_g and σ_k have a minimum value of 1 voxel [35], [57] and the curvature scale σ_h has a minimum value of 2.7 voxels for any sampling rate below 3× Nyquist rate [58].

For a number of parameters, a stable or linear regime was found in their value range. Within this regime, the parameter was optimized for computational time and other desirable features. Parameters with a stable regime were determined with a tuning algorithm. Initial parameters were chosen as a starting point, after which each parameter was tuned individually and the effect on the resulting image was quantified. Based on these results, the initial parameters were adjusted to the most optimal value in the stable or linear regime of the parameter. As a verification, the entire process was repeated with the adjusted parameters and the effect on the resulting image was quantified again. If needed, the parameters were adjusted and verified until robustness was accomplished.

2.2.7 Analysis of curvature-intensity correlation

Photon emission from a population of fluorescent emitters follows a Poisson distribution. As we did not record photon count n but normalized lamin B1 intensity i_{B1}, the intensity signal from the nuclear lamina was multiplied by a scaling factor c. The intensity measurements imply that $n \notin \mathbb{N}$, so the factorial of the Poisson distribution was approximated with a gamma function. The shape of Poisson distribution j is dependent on parameter μ_j and height h_j. The resulting Poisson function is shown in *formula 13* and describes the measured intensity spread of any population of fluorescent emitters. The sum of two Poisson functions was fitted on the intensity histogram of lamin B1. A non-linear least squares regression curve fit was used, as previously described in *section 2.2.1*. The two individual Poisson functions represent the two lamin B1 meshwork states described in *section 1.3*.

$$P_j(n) = h_j \frac{{\mu_j}^n e^{-\mu_j}}{n!}, n = c\, i_{B1} \quad (\mathbf{13})$$

The correlation between curvature of the nuclear lamina and the depletion of lamin B1 was found by studying the height change of the two Poisson functions for increasing curvatures. Firstly, the Gaussian curvature was computed from the principal curvatures with *formula 2*. All segmented voxels were sorted in bins with increasing Gaussian curvature. For each curvature bin, the intensity histogram for lamin B1 was computed. A new double Poisson function was fitted for each curvature bin by keeping parameters c and μ_j constant and only adjusting heights h_j. Poisson functions are inherently normalized as probability density functions, so the fraction of signal from the high-intensity population for each curvature bin was calculated with *formula 14*. This fraction, or so-called occupancy, corresponds to the probability P_{high} of the lamin B1 signal being in the high-intensity state at the specified curvature.

$$P_{\text{high}} = \frac{h_{\text{high}}}{h_{\text{high}} + h_{low}} \quad (\mathbf{14})$$

The sigmoid probability function of *formula 1* was fitted on the computed probabilities P_{high} by a non-linear least squares regression curve fit as previously described in *section 2.2.1*. For this curve fit, each point was also compensated by its standard error. This error was approximated by the binomial standard deviation σ_{bin} as described by *formula 15*, which depends on the probability P_{high} and voxel count N_{voxels} of the curvature bin. The fitted parameters for this curve fit were recorded and represent the different energy variables from *formula 1*.

$$\sigma_{\text{bin}} = \sqrt{\frac{P_{\text{high}}\,(1 - P_{\text{high}})}{N_{\text{voxels}}}} \quad (\mathbf{15})$$

3 Results

In this section, the results from the image analysis pipeline are described for the main dataset. First, we present robust parameter values for the dataset. Then, the application of curvature estimation and the robust parameter values are tested on artificial structures. Lastly, the full pipeline is applied on the main dataset and the results are shown. The main dataset provided 13 FOVs with a total of 76 segmented nuclei. The maximum intensities of lamin A/C and lamin B1 were combined to represent the nuclear lamina for labeling, segmentation and curvature computation. The largest excitation wavelength λ_{max} = 561 nm was considered to simulate the PSF of this representation, as previously shown in *figure 7*, resulting in isotropic blurring scale σ_{iso} = 0.14 µm.

3.1 Setting robust parameters

The data analysis pipeline required a number of parameters to be tuned. Here, we describe the parameter values found to be most robust. First, the optimal parameters for labeling and segmentation operations are described. This is followed by a section on optimal parameter values for the curvature estimation algorithm. It is important to note again that robust parameter values are highly dependent on dataset properties and should always be reconsidered for new datasets.

3.1.1 Labeling and segmentation parameters

We tuned the parameters discussed in the methods for optimal nuclear lamina labeling and segmentation. First, we determined the optimal value for the label expansion distance d. This parameter determines the range around each nucleus for which the curvature will be computed. To reduce computational time, it was considered optimal to limit this distance as much as possible. However, the computed curvature for the nuclear lamina also depends on intensities beyond the mask, which are required for derivative computation and subsequent blurring operations. Therefore, the label must be expanded over a large enough distance to allow for the inclusion of these neighboring intensities. We determined a robust value for d to be one that stabilized the mean absolute Gaussian curvature within the mask by fine segmentation of the nuclear lamina. The result is shown in *figure 14a* and the final value d = 4 µm was chosen.

There are three parameters to be set for the rough segmentation of the nuclear lamina: the blurring parameter σ_m, the cut-off intensity i_c and segmentation accuracy α. These parameters mainly influence the volume of the mask by rough segmentation. The parameters α and i_c have a range of 0 to 1, as they represent a compression factor and an intensity fraction, respectively. The mask volume grows by increasing σ_m and α or decreasing i_c. In the stable regime of these parameters, the volume of the mask is approximately linearly dependent on each parameter. This is referred to as the linear regime and shown in *figure 14b-d*. Minimizing σ_m reduces computational time, minimizing i_c closes holes in the mask and maximizing α increases the accuracy of the edges of the mask. However, for extreme values of σ_m, i_c and α, artifacts occur, causing a nonlinear change of the mask volume. Thus, optimal values for the segmentation parameters are found at the edges of their linear regimes. Robust parameters are set at σ_m = 0.9 µm, i_c = 0.25 of the maximum intensity of I_b and α = 0.9.

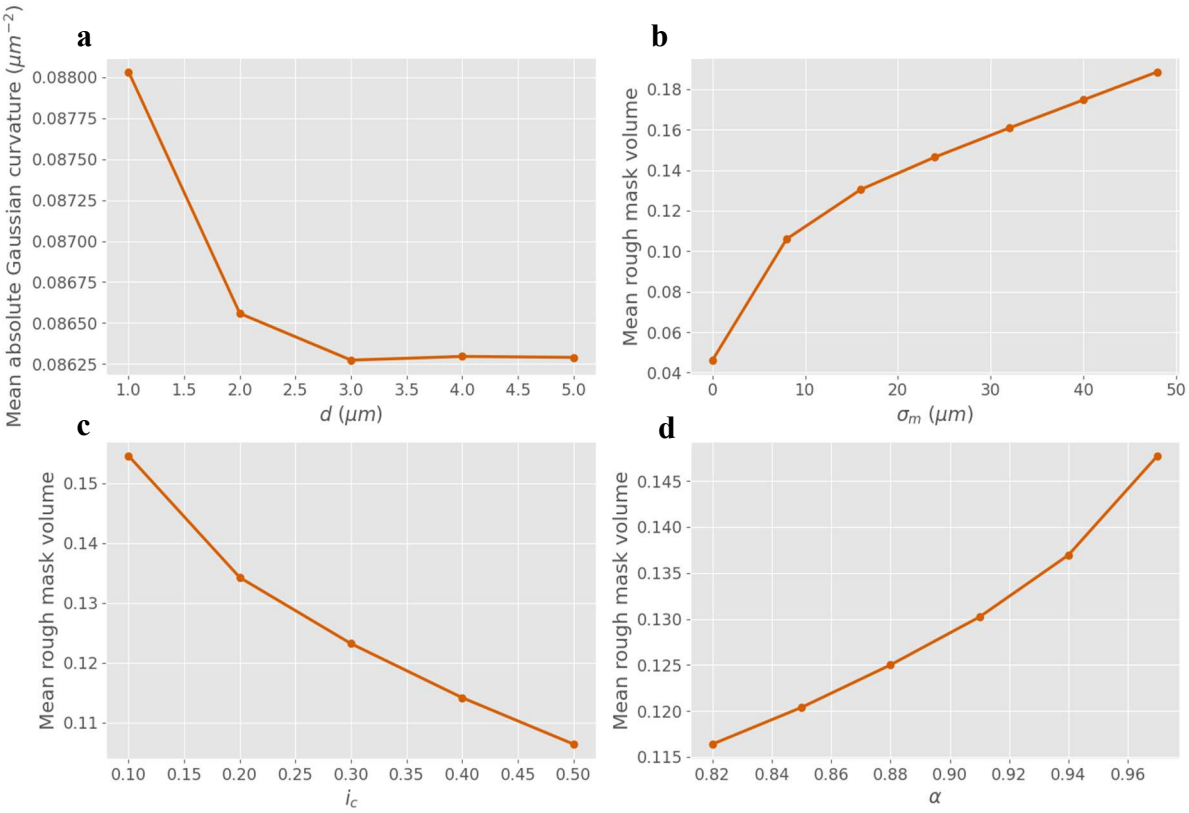

Figure 14. Robustness for labeling and segmentation parameter values. $N = 76$ nuclei. **a.** The mean absolute Gaussian curvature for the fine segmentation of the nuclear lamina for different values of parameter d. A robust value of $d = 4$ μm was chosen. **b-d.** The mean volume of the mask by rough segmentation as a fraction of the total image volume for different values of segmentation parameters. **b.** A robust value of $\sigma_m = 0.9$ μm was chosen. **c.** A robust value of $i_c = 0.25$ of the maximum intensity of $\boldsymbol{I}_b$ was chosen. **d.** A robust value of $\alpha = 0.9$ was chosen.

Fine segmentation of the nuclear lamina requires the additional parameter σ_s. The parameter σ_s represents the scale of the steerable filter which is used to detect the surface of the nuclear lamina. The mask volume by fine segmentation is not linearly dependent on this parameter, nor does the parameter show a stable regime. Therefore, the parameter was chosen based on the results of a typical dataset as shown in *figure 15*. Low values for σ_s created a webbing structure in the mask, caused by noise in the image. High values of σ_s shifted the detection of curved surfaces inwards. This is not desirable, as it causes the mask to move away from the maximum intensity ridge of the nuclear lamina. We found the optimal value to be $\sigma_s = 0.3$ μm.

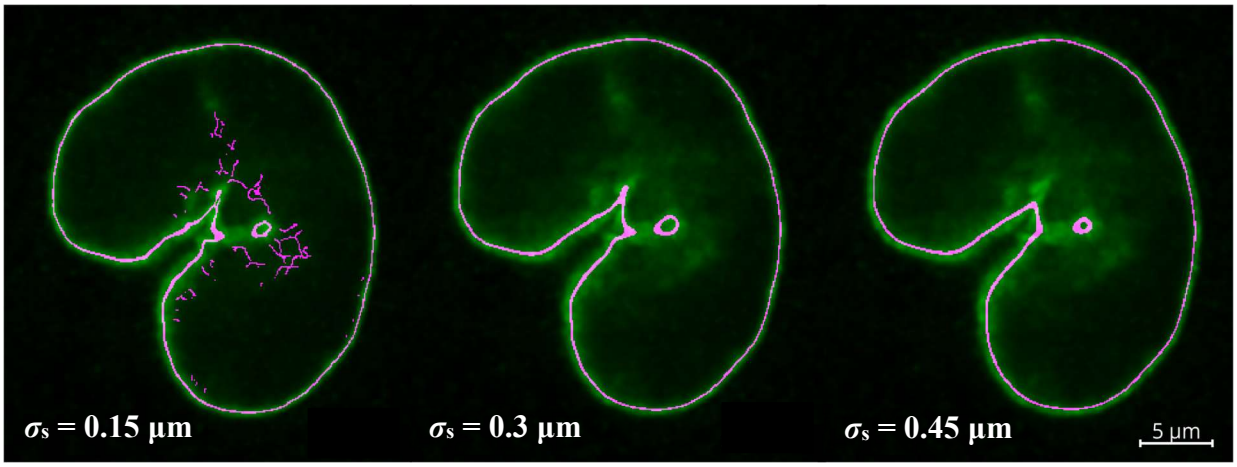

Figure 15. Cross-section of the nuclear lamina, in this case the maximum of lamin A/C and lamin B1 signal and depicted in green, with the mask by fine segmentation, depicted in magenta, for σ_s = 0.15 µm, σ_s = 0.3 µm and σ_s = 0.45 µm. We decided σ_s = 0.3 µm to be a robust value.

3.1.2 Curvature parameters

The computation of curvature involves a third set of parameters: the Gaussian kernel scales σ_g, σ_t and σ_k. These parameters determine the scale of gradient derivatives, GST blurring and normal vector derivatives, respectively. The lowest reasonable value for σ_g and σ_k is 1 voxel and gives the most accurate results as shown by previous studies [35], [57]. Thus, these parameters were set at $\sigma_g = \sigma_k = 0.090$ µm, which is the isotropic voxel size of the supplementary dataset in *appendix II*, to keep the scale for curvature computation constant between the main and supplementary datasets. The parameter σ_t determines the scale for the blurring operation on the GST matrix elements. Increasing this value results in decreased noise but also reduced detail. *Figure 16* shows a typical dataset for three values of σ_t and based on these results, an optimal value of σ_t = 0.4 µm was chosen. The parameter σ_h can be derived from these three parameters as previously described in *formula 10* and results in σ_h = 0.420 µm. This meets both the minimum requirement of 2.7 voxels [58], as it is larger than 0.183 µm, and the maximum requirement calculated with *formula 9*, as it is below R_{min} = 0.565 µm.

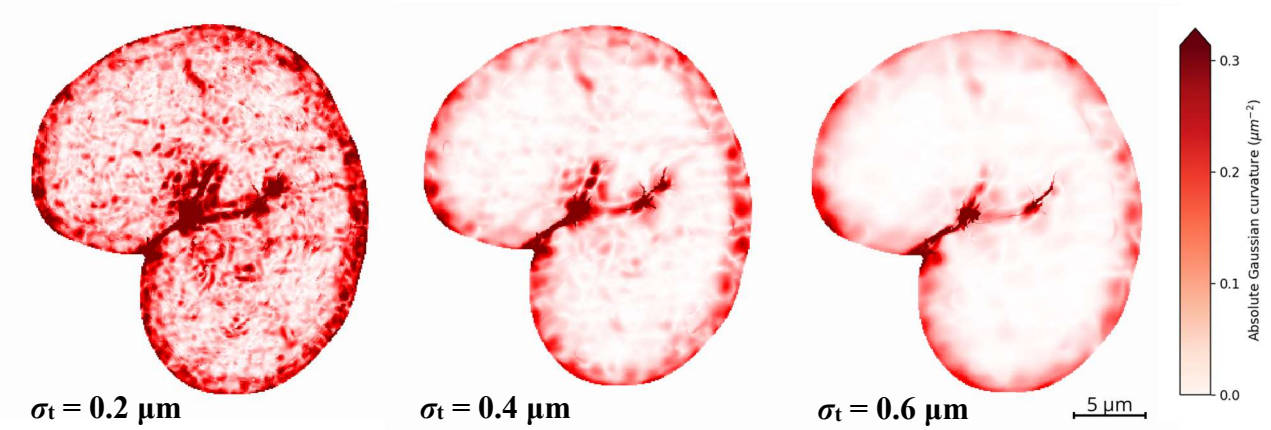

Figure 16. Maximum intensity projections of the absolute Gaussian curvature of the nuclear lamina for σ_t = 0.2 µm, σ_t = 0.4 µm and σ_t = 0.6 µm. We decided σ_t = 0.4 µm to be a robust value.

3.2 Testing on artificial structures

Artificial structures were used to validate the image analysis pipeline and the robust parameters found in *section 3.1*. The artificial structures have dimensions similar to the nuclei of HeLa cells, and voxel size of 0.061×0.061×0.061 µm identical to the isotropic voxel size of the dataset. Anti-aliasing was applied to smoothen the edges of the binary representations and the structures were subsequently blurred with σ_{iso} = 0.14 µm to resemble the isotropic PSF of the datasets. The robust parameters from *section 3.1* were used for the analysis pipeline.

Firstly, the curvature of a hollow sphere was computed. The cross-section of a hollow sphere is shown in *figure 17a* with the computed curvatures for its rough segmentation in *figure 17b*. As can be seen, the Gaussian curvature slightly increases internally, because the corresponding radius of curvature decreases. The theoretical curvature for this hollow sphere is 0.041 µm^{-2}, which was computed from its average radius using *formula 2*. As shown in *figure 17b*, the computed curvatures closely resemble this theoretical curvature.

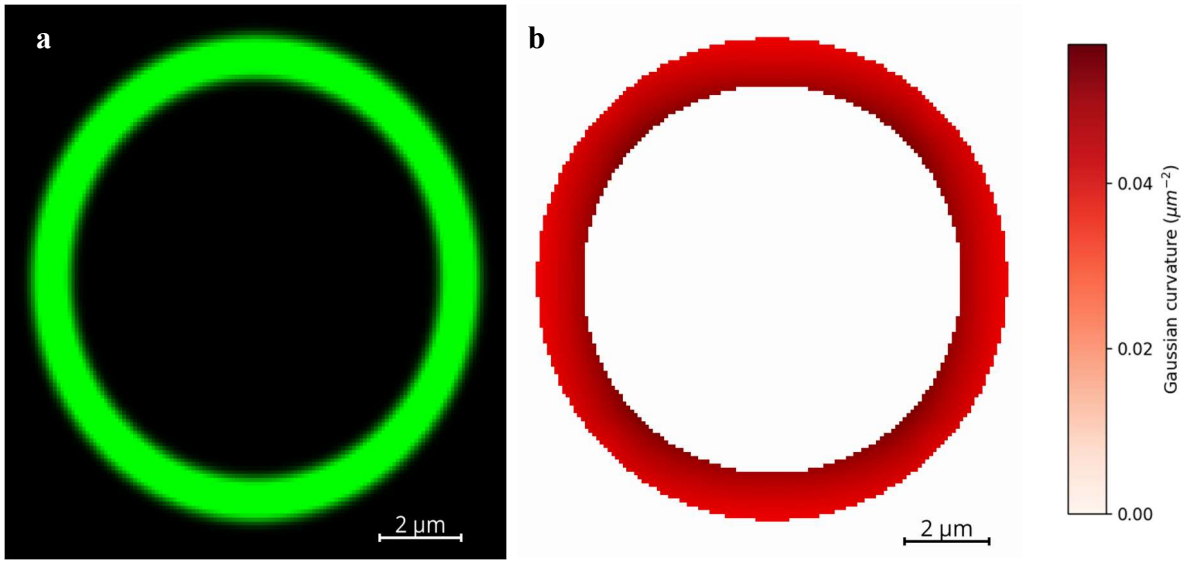

Figure 17. Anti-aliased hollow sphere blurred with σ_{iso} = 0.14 µm to test curvature computation. **a.** Cross-section of hollow sphere used to test curvature computation. **b.** The computed curvature for the rough segmentation of the cross-section of the hollow sphere. The theoretical curvature is 0.041 µm^{-2}.

Secondly, the curvature of a hollow torus was computed to validate the sign recovery procedure. The hollow torus and its lateral cross-section are shown in *figure 18a* and *figure 18b*, respectively. *Figure 18c* shows the computed Gaussian curvature for this hollow torus. The theoretical inner curvature is -0.165 µm^{-2} and the theoretical outer curvature is 0.091 µm^{-2}. As shown in *figure 18c*, the computed curvatures closely resemble these theoretical curvatures.

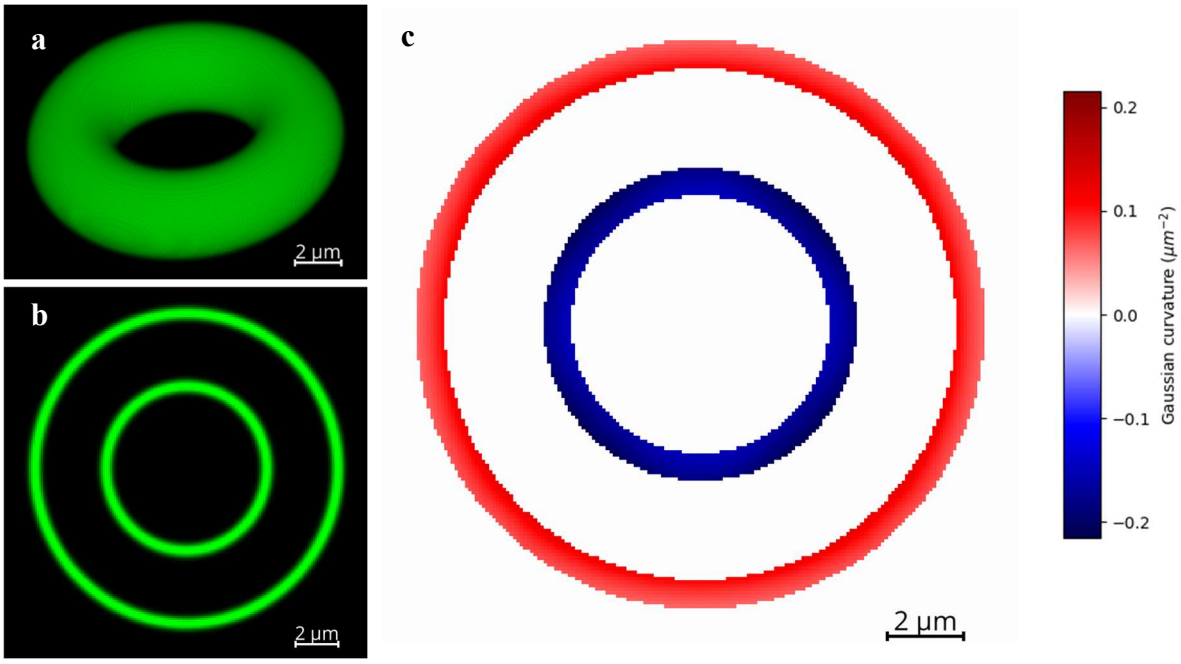

Figure 18. Anti-aliased hollow torus blurred with σ_{iso} = 0.14 µm to test the sign recovery procedure. **a.** Three-dimensional representation of hollow torus. **b.** Lateral cross-section of hollow torus. **c.** The computed curvature for the rough segmentation of the cross-section of the hollow torus. The theoretical inner curvature is -0.165 μm^{-2} and the theoretical outer curvature is 0.091 μm^{-2}.

3.3 Absolute Gaussian curvature and lamin B1 intensity

Sign recovery for principal curvatures is not applied for the main results analysis, because the quality of sign recovery was not sufficient. As shown in *figure 19a*, DNA frequently did not form a uniform and solid representation for a nucleus, especially for mitotic cell nuclei. Many of these nuclei contain condensed chromosomes resulting in an uneven distribution of DNA throughout the nucleus and thus an irregular shape of the recorded DAPI signal. The irregular shape causes the detection of negative isophote curvature where there is none as shown in *figure 19b*. A supplementary analysis of the main dataset including sign recovery is presented in *appendix I*.

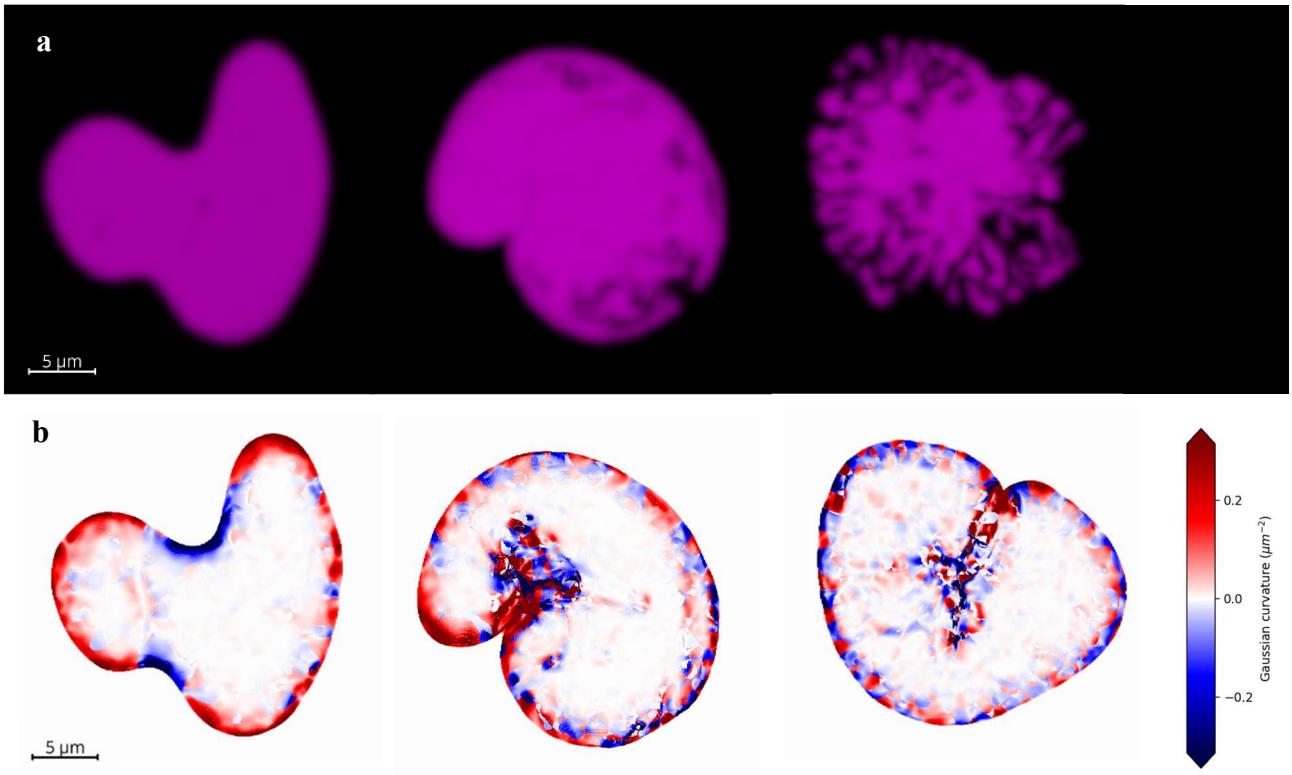

Figure 19. Signal from DNA and the computed Gaussian curvature for several nuclei, ranging from relatively accurate to inaccurate sign recovery due to decreasing quality of sign recovery. **a.** Three-dimensional representation of DNA inside the nucleus by attenuated maximum intensity projection of processed DAPI signal. **b.** Maximum intensity projection of computed Gaussian curvature for the nuclear lamina.

We analyzed the relation between absolute Gaussian curvature and lamin B1 intensities for the fine segmentation of the nuclear lamina for all recorded nuclei. Based on *formula 8* and our microscope characteristics from *section 2.1*, we determined the upper computation limit for the principal curvatures in this dataset to be $|\kappa_{max}|$ = 1.769 µm^{-1}. Filtering out all voxels with absolute principal curvatures exceeding this value, reduced the dataset by 1.7%. From these filtered principal curvatures, the absolute Gaussian curvature was computed using *formula 2*. *Figure 20a* shows a logarithmic two-dimensional histogram of the absolute Gaussian curvature and intensity of the filtered dataset, with the mean, median and upper 95th percentile intensities at all curvatures. *Figure 20b* shows the total intensity histogram of the filtered dataset and *figure 20c* shows the logarithmic total absolute Gaussian curvature histogram of the filtered dataset.

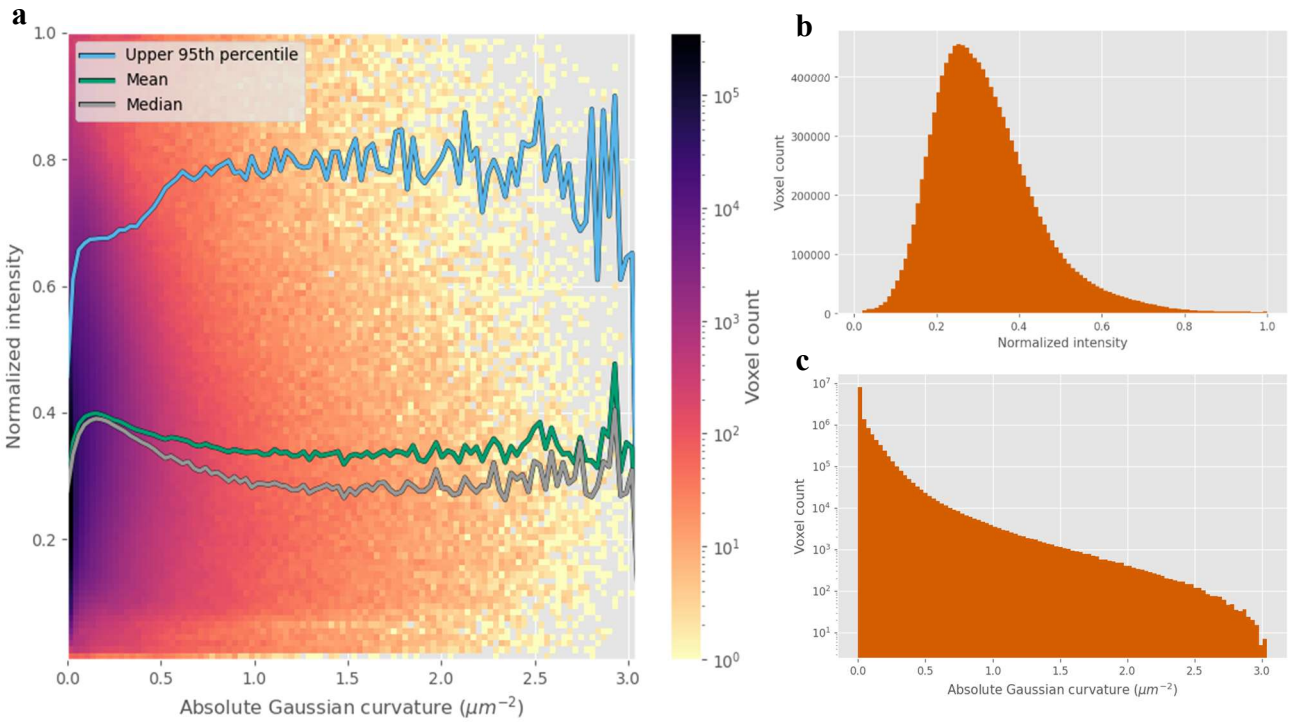

Figure 20. Absolute Gaussian curvature and lamin B1 intensity for the fine segmentation of the nuclear lamina, filtered with $|\kappa_{max}|$ = 1.769 µm^{-1}. N = 12 909 976 voxels. **a.** Two-dimensional histogram for absolute Gaussian curvature and normalized lamin B1 intensity, with the mean, median and upper 95th percentile intensities for all curvatures. **b.** The total intensity histogram for the filtered dataset. **c.** The total absolute Gaussian curvature histogram for the filtered dataset.

Since we are particularly interested in higher curvature regions, we focus on higher curvature data only. Therefore, the absolute Gaussian curvature was restricted with a lower curvature limit of 0.15 μm^{-2}. This restriction reduced the total dataset by another 86.9%. The decision to exclude absolute Gaussian curvatures below 0.15 μm^{-2} was based on two observations. Firstly, *figure 20a* shows that intensity statistics dramatically shift for this curvature range. Secondly, *figure 21* shows that the intensity histograms of these two curvature ranges differ a lot and no double Poisson distribution can be found for the low-curvature intensity histogram. Because there is a high quantity of low-curvature data, this data would obscure the double Poisson distribution that is present for higher curvatures. Assuming *formula 1*, the intensity of lamin B1 at low curvatures is not governed by the amount of curvature and thus does not need to be considered when studying the correlation between curvature and intensity.

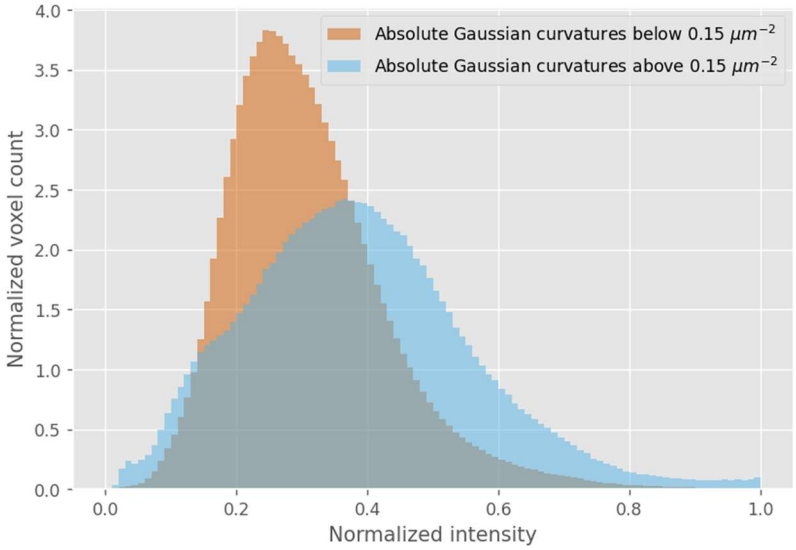

Figure 21. Comparison of normalized intensity histograms for absolute Gaussian curvatures below and above 0.15 μm^{-2}. A double Poisson distribution can be found for high-curvature intensities but not for low-curvature intensities. N = 11 418 604 voxels for low curvatures and N = 1 491 372 voxels for high curvatures.

The double Poisson function was fitted on the total intensity histogram of the reduced dataset as shown in *figure 22a*. For the probability function described by *formula 1*, parameters l_p = 0.38 µm and L_{fil} = 0.5 µm were used based on the theory of *section 1.2* [21], [32] and binomial standard deviations were computed as described by *formula 15*. The fraction of high-intensity voxels for each curvature, the so-called occupancy, and the fitted probability model following *formula 1* are shown in *figure 22b*. The cut-off Gaussian curvature K_c was computed with the ratio E/a = 0.69 μm^{-1}, as described in *section 1.3* and by *formula 2,* resulting in K_c = 0.48 μm^{-2}. The majority of lamin B1 depletion occurs around the cut-off Gaussian curvature K_c, between the absolute Gaussian curvatures 0.2 μm^{-2} and 0.8 μm^{-2}. The upper and lower bound for the sigmoid probability function in *figure 22b* are A = 0.96 and B = 0.41, respectively. These bounds imply that the occupancy of the high-intensity population is 96% for the low-curvature regime and 41% for the high-curvature regime. *Figure 22c* shows the intensity histogram and fitted Poisson functions for several curvature ranges between 0.15 μm^{-2} and 0.90 μm^{-2} to illustrate the occupancy change for this critical curvature range.

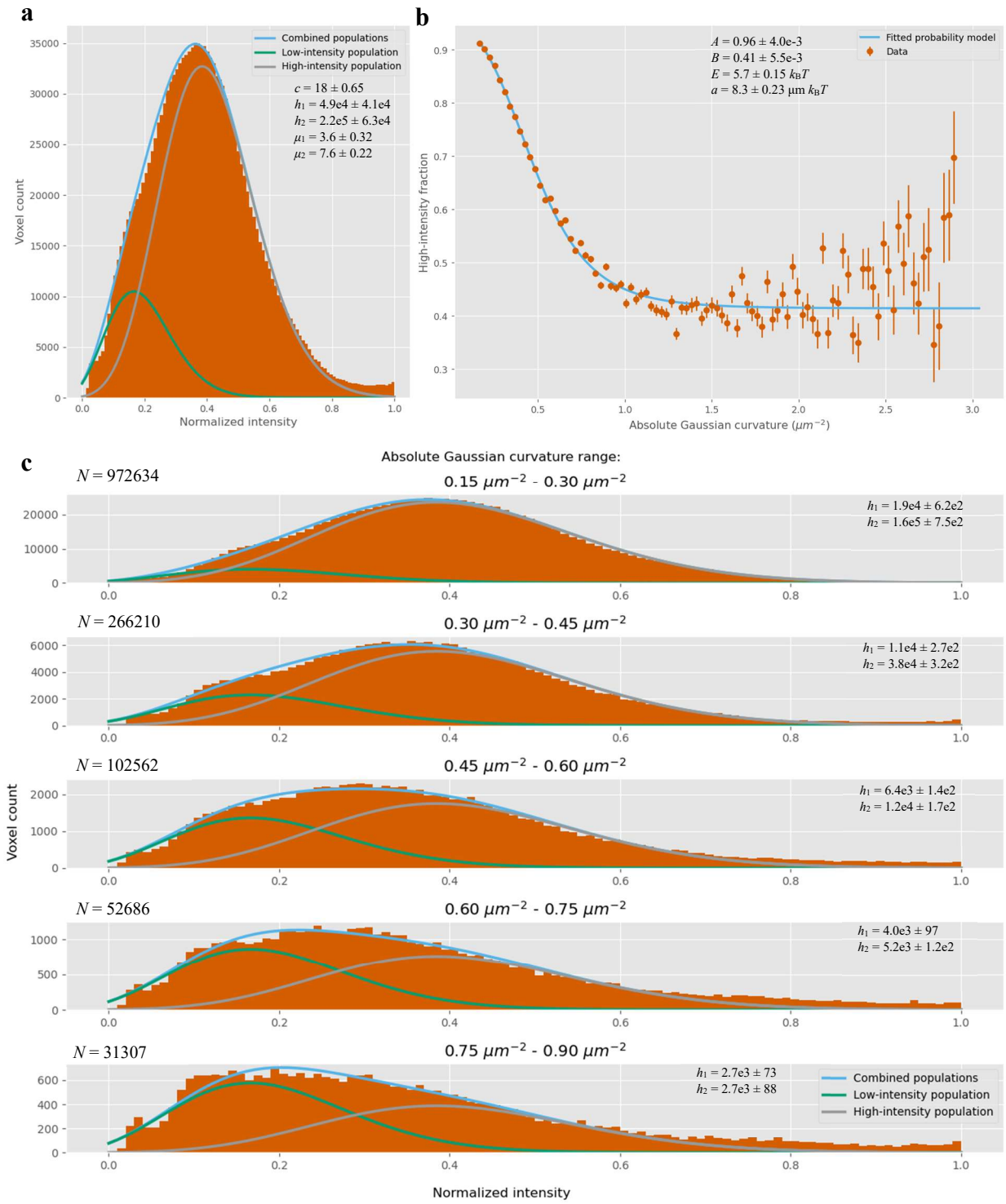

Figure 22. Intensity histograms and fitted probability model for the dataset, filtered with $|\kappa_{max}|$ = 1.769 μm^{-1} and restricted with a lower absolute Gaussian curvature limit of 0.15 μm^{-2}. N = 1 491 372 voxels. **a.** Total intensity histogram with the fitted double Poisson function and component Poisson functions as described in *formula 13*. **b.** The occupancy of the high-intensity population, with standard deviations as described in *formula 15*, with the fitted probability model as described in *formula 1*. **c.** Intensity histograms for several curvature ranges with the fitted double Poisson function and component Poisson functions as described in *formula 13*. Total voxel count N is noted at each histogram.

4 Conclusion and discussion

This thesis provides a reliable quantitative image analysis pipeline to test the relation between the curvature of the nuclear lamina and signal intensity in three-dimensional images. The results of this thesis also reveal a connection between Gaussian curvature of the nuclear lamina and its depletion of lamin B1 intensity following a two-state distribution, as hypothesized in *section 1.3*. Whereas previous studies have set the groundwork for the probability distribution model that corresponds to our data, we report for the first time a bimodal distribution as a consequence of curvature [18], [19]. First, we discuss this depletion model for the lamin B1 meshwork and its implications on the current knowledge of the nuclear lamina. Then, the robustness of pipeline parameters and the limitations of the applied image analysis pipeline are discussed. Finally, we describe recommendations for future studies based on the work presented in this thesis.

4.1 Lamin B1 depletion at high curvatures

We have found a bimodal distribution of lamin B1 intensity that correlates to curvature of the nuclear lamina. The high-intensity population in this distribution is considered an undisturbed, high-density lamin B1 meshwork and the low-intensity population is considered a low-density or depleted lamin B1 meshwork disturbed by curvature of the nuclear envelope. It is shown that for increasing curvature of the nuclear lamina, the lamin B1 meshwork shifts from the high-density state to the low-density or depleted state. This shift follows the probability model described by *formula 1*. The fitted parameters for the probability model are $E = 5.7\ k_BT$ and $a = 8.3\ \mu m\ k_BT$ as previously shown in *figure 22b*. These values resemble those found in other studies, which range between $E = 4.7\ k_BT – 5.1\ k_BT$ and $a = 8.2\ \mu m\ k_BT – 20\ \mu m\ k_BT$ [18], [19]. Additionally, the cut-off Gaussian curvature $K_c = 0.48\ \mu m^{-2}$ resembles the computed values from prior studies, which range between $K_c = 0.05\ \mu m^{-2} – 0.40\ \mu m^{-2}$ [18], [19]. The analyzed dataset shows a slightly slower decline of undisturbed lamin B1 quantity for increasing curvatures. This difference can be caused by biological differences between datasets, such as staining quality or variations in gene expression. The results of each study can also be influenced by data acquisition, such as PSF extend or voxel size.

The morphologies of the two different intensity states of the lamin B1 meshwork are still unclear. It is possible that the low-intensity state represents full depletion of lamin B1, or it could represent a disturbed lamin meshwork with lower lamin B1 density. The latter is supported by the observation that the low-intensity lamin B1 state still shows a relatively high mean intensity $\mu_1 = 3.6$. If the low-intensity state was fully depleted from lamin B1, we would expect its mean to be closer to 0. Such a disturbed low-density state would be able to replace the high-density state at high-curvature locations in the nuclear envelope. The low-density state would also be less stable, as high-curvature regions in the nuclear lamina show more ruptures [17], [18], [19]. Another possible explanation for the high mean intensity could be the existence of small patches of stable high-intensity meshwork at high-curvature locations. The latter is supported by the occupancy of 41% for the high-density state in the high-curvature regime.

The observed curvature dependency of the lamin B1 density provides new insight into the mechanisms regulating the structural integrity of the nuclear lamina. The quantity of lamin B1 influences the rigidity of the nuclear envelope [11], [33] and the structure of other lamin meshworks [25], [26]. Therefore, curvature of the nuclear envelope must play an important role in the regulation of mechanical support for the nucleus. Additionally, curvature might be a relevant factor during the initiation of NEBD, by weakening the nuclear lamina. The mitotic invagination described in *section 1.1* might be a cellular process to accelerate NEBD by applying additional curvature on the nuclear lamina to deplete and destabilize the lamin B1 meshwork, and subsequently rupture the nuclear lamina.

4.2 Robustness and limitations of data analysis

The obtained segmentation parameters in *section 3.1.1* are in agreement with prior literature, showing the validity of our segmentation pipeline and parameter determination procedure [36]. The blurring scale σ_m = 0.9 µm is equal to the previously proposed axial blurring scale, but much larger than the previously proposed lateral blurring scale of 0.06 µm. However, since our images were made isotropic before further analysis using the axial PSF extend, only the axial blurring scale provides a relevant comparison. The cut-off intensity i_c = 0.25 is lower than the previously proposed value i_c = 0.33. A lower value for i_c closes any potential holes and broadens the mask, thereby increasing the volume of the mask. In this case, a lower value for i_c was advantageous, as the rough segmentation was later combined with the fine segmentation. This combination nullified any extra width of the rough segmentation, but retained the additional closure of holes. The segmentation accuracy α = 0.9 is identical to the proposed value and appears to be effective for rough segmentation of the nuclear lamina.

The main limitation of the described image analysis pipeline is the need for a base level of intensity from the nuclear lamina. Any areas in the nuclear lamina without signal from lamin A/C or lamin B1 are not segmented. Additionally, curvature computation for these areas is unreliable, as the curvature is estimated from the local grey-scale values. This limitation creates a bias for areas in the nuclear lamina where lamin signal is present. The bias results in the exclusion of low-density patches and holes in the nuclear lamina and reduces the overall quantity of low-intensity data. This reduction possibly causes the relatively high mean intensity μ_1 = 3.6 of the low-density lamin B1 state and the relatively high occupancy of 41% for the high-density lamin B1 state at high curvatures as mentioned in *section 4.1*. The curvature and lamin B1 density at the missing low-intensity areas would be of particular importance to the results of this thesis, as they could provide insight into the effect of curvature on low lamin B1 densities.

Using the MIP of the nuclear lamina for the labeling of nuclei caused an additional limitation. Where two nuclei overlap or are directly adjacent, they could not be distinguished. Watershed segmentation proved to be inadequate to address this issue, as the nucleus shape and signal intensity were too irregular. The resulting fusion of nuclei had two unwanted consequences. Firstly, normalization is applied over the set of fused nuclei instead of the individual nuclei. Secondly, the curvature of the fused nuclear lamina is analyzed instead of the individual nuclear lamina. This can result in the computation of extreme curvatures at the locations where the nuclear lamina of two cells are fused. However, neither consequence likely had a significant impact on the global dataset analysis, as most nuclei had a comparable maximum intensity and curvature computation was only affected at very small, localized regions.

The parameters L_{fil} = 0.5 μm and l_p = 0.38 μm for the probability model, previously mentioned in *section 3.3*, are based on the most commonly observed quantities in physical studies [21], [32]. These quantities are not very exact and, especially for l_p, a range of previously recorded lengths exists. However, the entire bending energy term in *formula 1* is relatively insignificant to the final shape of the sigmoid probability function. The binding energy term contributes a lot more to the exponential term due to its dependence on $\sqrt{K}$ instead of K. The relative uncertainty for the values of parameters L_{fil} and l_p can therefore be deemed irrelevant to the final results.

4.3 Recommendations for future research

This thesis provides a deeper understanding of the structure of the nuclear lamina. However, further research is needed into the function of curvature during initiation of NEBD. Additional curvature might be induced by nuclear envelope structures like the mitotic invagination discussed in *section 1.1*. This added curvature does not seem to be required for successful cell division, but it might play a vital role in the accelerated breakdown of the nuclear lamina and subsequent NEBD. Moreover, little to no studies cover the curvature dependency of other lamin isoforms. It is known that lamin A/C depletion is mostly dependent on strain rate of curvature instead of curvature quantity [17], [19], but no depletion model has been proposed for this meshwork yet. Lamin B2 is severely understudied and more studies are needed to uncover its role in the structural integrity of the nuclear lamina.

More research is needed to further investigate the lamin B1 meshwork and its behavior for high curvature of the nuclear lamina. The analysis of negative Gaussian curvature in this thesis is limited and a more effective way to recover the sign of curvature is required, for example by using a better three-dimensional solid representation of the nucleus. There are approaches to obtain this solid representation from the nuclear lamina, requiring a completely closed shell, which was not the case for many nuclei in our dataset [59]. Creating a closed shell representation for the nuclear lamina would also eliminate the bias for high intensities described in *section 4.2*. Additionally, future research could investigate the physical properties behind the fitted parameters for the probability model described in *formula 1*, such as the binding energy of the lamin B1 meshwork. Lastly, further studies can elaborate on other processes that cause density differences for lamin B1. *Figure 21* shows a distinct intensity histogram for lamin B1 at curvatures below 0.15 μm^{-2}, where lamin B1 density is possibly governed by a different process. Moreover, the disturbed state of the lamin B1 meshwork might represent a novel low-density meshwork state and more research is necessary to investigate this possibility. This thesis lays a solid foundation for any of the future research directions discussed.

Bibliography

[1] L. Guelen *et al.*, “Domain organization of human chromosomes revealed by mapping of nuclear lamina interactions,” *Nature*, vol. 453, no. 7197, pp. 948–951, Jun. 2008, doi: 10.1038/nature06947.

[2] J. M. Zullo *et al.*, “DNA Sequence-Dependent Compartmentalization and Silencing of Chromatin at the Nuclear Lamina,” *Cell*, vol. 149, no. 7, pp. 1474–1487, Jun. 2012, doi: 10.1016/j.cell.2012.04.035.

[3] A. Vahabikashi *et al.*, “Nuclear lamin isoforms differentially contribute to LINC complex-dependent nucleocytoskeletal coupling and whole-cell mechanics,” *Proc. Natl. Acad. Sci.*, vol. 119, no. 17, p. e2121816119, Apr. 2022, doi: 10.1073/pnas.2121816119.

[4] M. Crisp *et al.*, “Coupling of the nucleus and cytoplasm: Role of the LINC complex,” *J. Cell Biol.*, vol. 172, no. 1, pp. 41–53, Dec. 2005, doi: 10.1083/jcb.200509124.

[5] M. Kittisopikul *et al.*, “Computational analyses reveal spatial relationships between nuclear pore complexes and specific lamins,” *J. Cell Biol.*, vol. 220, no. 4, p. e202007082, Feb. 2021, doi: 10.1083/jcb.202007082.

[6] J. Swift *et al.*, “Nuclear Lamin-A Scales with Tissue Stiffness and Enhances Matrix-Directed Differentiation,” *Science*, vol. 341, no. 6149, p. 1240104, Aug. 2013, doi: 10.1126/science.1240104.

[7] G. Bonne *et al.*, “Mutations in the gene encoding lamin A/C cause autosomal dominant Emery-Dreifuss muscular dystrophy,” *Nat. Genet.*, vol. 21, no. 3, pp. 285–288, Mar. 1999, doi: 10.1038/6799.

[8] H. Cao and R. A. Hegele, “Nuclear lamin A/C R482Q mutation in Canadian kindreds with Dunnigan-type familial partial lipodystrophy,” *Hum. Mol. Genet.*, vol. 9, no. 1, pp. 109–112, Jan. 2000, doi: 10.1093/hmg/9.1.109.

[9] Q. S. Padiath *et al.*, “Lamin B1 duplications cause autosomal dominant leukodystrophy,” *Nat. Genet.*, vol. 38, no. 10, pp. 1114–1123, Oct. 2006, doi: 10.1038/ng1872.

[10] A. De Sandre-Giovannoli *et al.*, “Homozygous Defects in LMNA, Encoding Lamin A/C Nuclear-Envelope Proteins, Cause Autosomal Recessive Axonal Neuropathy in Human (Charcot-Marie-Tooth Disorder Type 2) and Mouse,” *Am. J. Hum. Genet.*, vol. 70, no. 3, pp. 726–736, Mar. 2002, doi: 10.1086/339274.

[11] M. Eriksson *et al.*, “Recurrent de novo point mutations in lamin A cause Hutchinson–Gilford progeria syndrome,” *Nature*, vol. 423, no. 6937, pp. 293–298, May 2003, doi: 10.1038/nature01629.

[12] A. Vahabikashi, S. A. Adam, O. Medalia, and R. D. Goldman, “Nuclear lamins: Structure and function in mechanobiology,” *APL Bioeng.*, vol. 6, no. 1, p. 011503, Mar. 2022, doi: 10.1063/5.0082656.

[13] B. Lüscher, L. Brizuela, D. Beach, and R. N. Eisenman, “A role for the p34cdc2 kinase and phosphatases in the regulation of phosphorylation and disassembly of lamin B2 during the cell cycle.,” *EMBO J.*, vol. 10, no. 4, pp. 865–875, Apr. 1991, doi: 10.1002/j.1460-2075.1991.tb08019.x.

[14] Y. Ottaviano and L. Gerace, “Phosphorylation of the nuclear lamins during interphase and mitosis.,” *J. Biol. Chem.*, vol. 260, no. 1, pp. 624–632, Jan. 1985, doi: 10.1016/S0021-9258(18)89778-2.

[15] J. Beaudouin, D. Gerlich, N. Daigle, R. Eils, and J. Ellenberg, “Nuclear Envelope Breakdown Proceeds by Microtubule-Induced Tearing of the Lamina,” *Cell*, vol. 108, no. 1, pp. 83–96, Jan. 2002, doi: 10.1016/S0092-8674(01)00627-4.

[16] D. Salina, K. Bodoor, D. M. Eckley, T. A. Schroer, J. B. Rattner, and B. Burke, "Cytoplasmic dynein as a facilitator of nuclear envelope breakdown," *Cell*, vol. 108, no. 1, pp. 97–107, Jan. 2002, doi: 10.1016/s0092-8674(01)00628-6.
[17] B. Nmezi *et al.*, "Concentric organization of A- and B-type lamins predicts their distinct roles in the spatial organization and stability of the nuclear lamina," *Proc. Natl. Acad. Sci.*, vol. 116, no. 10, pp. 4307–4315, Mar. 2019, doi: 10.1073/pnas.1810070116.
[18] Y. Xia *et al.*, "Rescue of DNA damage after constricted migration reveals a mechano-regulated threshold for cell cycle," *J. Cell Biol.*, vol. 218, no. 8, pp. 2545–2563, Aug. 2019, doi: 10.1083/jcb.201811100.
[19] C. R. Pfeifer *et al.*, "Gaussian curvature dilutes the nuclear lamina, favoring nuclear rupture, especially at high strain rate," *Nucleus*, vol. 13, no. 1, pp. 130–144, Dec. 2022, doi: 10.1080/19491034.2022.2045726.
[20] J. Lippincott-Schwartz, "Ripping up the nuclear envelope," *Nature*, vol. 416, no. 6876, pp. 31–32, Mar. 2002, doi: 10.1038/416031a.
[21] Y. Turgay *et al.*, "The molecular architecture of lamins in somatic cells," *Nature*, vol. 543, no. 7644, pp. 261–264, Mar. 2017, doi: 10.1038/nature21382.
[22] F. Lin and H. J. Worman, "Structural organization of the human gene encoding nuclear lamin A and nuclear lamin C," *J. Biol. Chem.*, vol. 268, no. 22, pp. 16321–16326, Aug. 1993, doi: 10.1016/S0021-9258(19)85424-8.
[23] F. Lin and H. J. Worman, "Structural Organization of the Human Gene (LMNB1) Encoding Nuclear Lamin B1," *Genomics*, vol. 27, no. 2, pp. 230–236, May 1995, doi: 10.1006/geno.1995.1036.
[24] M. Giacca *et al.*, "Fine mapping of a replication origin of human DNA," *Proc. Natl. Acad. Sci. U. S. A.*, vol. 91, no. 15, pp. 7119–7123, Jul. 1994, doi: 10.1073/pnas.91.15.7119.
[25] T. Shimi *et al.*, "The A- and B-type nuclear lamin networks: microdomains involved in chromatin organization and transcription," *Genes Dev.*, vol. 22, no. 24, pp. 3409–3421, Dec. 2008, doi: 10.1101/gad.1735208.
[26] T. Shimi *et al.*, "Structural organization of nuclear lamins A, C, B1, and B2 revealed by superresolution microscopy," *Mol. Biol. Cell*, vol. 26, no. 22, pp. 4075–4086, Nov. 2015, doi: 10.1091/mbc.E15-07-0461.
[27] R.-A. Röber, K. Weber, and M. Osborn, "Differential timing of nuclear lamin A/C expression in the various organs of the mouse embryo and the young animal: a developmental study," *Development*, vol. 105, no. 2, pp. 365–378, Feb. 1989, doi: 10.1242/dev.105.2.365.
[28] C. F. Lehner, R. Stick, H. M. Eppenberger, and E. A. Nigg, "Differential expression of nuclear lamin proteins during chicken development.," *J. Cell Biol.*, vol. 105, no. 1, pp. 577–587, Jul. 1987, doi: 10.1083/jcb.105.1.577.
[29] S. A. Adam, V. Butin-Israeli, M. M. Cleland, T. Shimi, and R. D. Goldman, "Disruption of lamin B1 and lamin B2 processing and localization by farnesyltransferase inhibitors," *Nucleus*, vol. 4, no. 2, pp. 142–150, Mar. 2013, doi: 10.4161/nucl.24089.
[30] E. Figueiras, O. F. Silvestre, T. O. Ihalainen, and J. B. Nieder, "Phasor-assisted nanoscopy reveals differences in the spatial organization of major nuclear lamina proteins," *Biochim. Biophys. Acta BBA - Mol. Cell Res.*, vol. 1866, no. 12, p. 118530, Dec. 2019, doi: 10.1016/j.bbamcr.2019.118530.
[31] L. A. Murray-Nerger and I. M. Cristea, "Lamin post-translational modifications: emerging toggles of nuclear organization and function," *Trends Biochem. Sci.*, vol. 46, no. 10, pp. 832–847, Oct. 2021, doi: 10.1016/j.tibs.2021.05.007.
[32] J. Mahamid *et al.*, "Visualizing the molecular sociology at the HeLa cell nuclear periphery," *Science*, vol. 351, no. 6276, pp. 969–972, Feb. 2016, doi: 10.1126/science.aad8857.

[33] O. Wintner *et al.*, “A Unified Linear Viscoelastic Model of the Cell Nucleus Defines the Mechanical Contributions of Lamins and Chromatin,” *Adv. Sci.*, vol. 7, no. 8, p. 1901222, 2020, doi: 10.1002/advs.201901222.
[34] R. Vaillant, *Curvature of a triangle mesh, definition and computation*. Accessed: May 28, 2025. [Online]. Available: https://rodolphe-vaillant.fr/entry/33/curvature-of-a-triangle-mesh-definition-and-computation
[35] B. Rieger, F. J. Timmermans, L. J. van Vliet, and P. W. Verbeek, “Curvature estimation of surfaces in 3D grey-value images,” in *2002 International Conference on Pattern Recognition*, Aug. 2002, pp. 684–687 vol.1. doi: 10.1109/ICPR.2002.1044847.
[36] C. H. Righolt, V. Raz, B. J. Vermolen, R. W. Dirks, H. J. Tanke, and I. T. Young, “Molecular Image Analysis: Quantitative Description and Classification of the Nuclear Lamina in Human Mesenchymal Stem Cells,” *Int. J. Mol. Imaging*, vol. 2011, no. 1, p. 723283, 2011, doi: 10.1155/2011/723283.
[37] L. J. van Vliet and P. W. Verbeek, “Curvature and Bending Energy in Digitized 2D and 3D Images,” in *SCIA’93*, Tromso, Norway, 1993.
[38] W. F. Scherer, J. T. Syverton, and G. O. Gey, “STUDIES ON THE PROPAGATION IN VITRO OF POLIOMYELITIS VIRUSES,” *J. Exp. Med.*, vol. 97, no. 5, pp. 695–710, May 1953, doi: 10.1084/jem.97.5.695.
[39] *Microscope - Imaging, Fluorescence, Resolution*. Accessed: May 30, 2025. [Online]. Available: https://www.britannica.com/technology/microscope/Confocal-microscopes
[40] J. Schindelin *et al.*, “Fiji: an open-source platform for biological-image analysis,” *Nat. Methods*, vol. 9, no. 7, pp. 676–682, Jul. 2012, doi: 10.1038/nmeth.2019.
[41] M. Linkert *et al.*, “Metadata matters: access to image data in the real world,” *J. Cell Biol.*, vol. 189, no. 5, May 2010, doi: 10.1083/jcb.201004104.
[42] G. van Rossum, “Python tutorial: Centrum voor Wiskunde en Informatica Amsterdam.” 1995. Accessed: May 22, 2025. [Online]. Available: https://cir.nii.ac.jp/crid/1370302866851079684
[43] C. R. Harris *et al.*, “Array programming with NumPy,” *Nature*, vol. 585, no. 7825, pp. 357–362, Sep. 2020, doi: 10.1038/s41586-020-2649-2.
[44] S. van der Walt *et al.*, “scikit-image: image processing in Python,” *PeerJ*, vol. 2, p. e453, Jun. 2014, doi: 10.7717/peerj.453.
[45] P. Virtanen *et al.*, “SciPy 1.0: fundamental algorithms for scientific computing in Python,” *Nat. Methods*, vol. 17, no. 3, pp. 261–272, Mar. 2020, doi: 10.1038/s41592-019-0686-2.
[46] S. K. Lam, A. Pitrou, and S. Seibert, “Numba: a LLVM-based Python JIT compiler,” in *Proceedings of the Second Workshop on the LLVM Compiler Infrastructure in HPC*, in LLVM ’15. New York, NY, USA: Association for Computing Machinery, Nov. 2015, pp. 1–6. doi: 10.1145/2833157.2833162.
[47] J. D. Hunter, “Matplotlib: A 2D Graphics Environment,” *Comput. Sci. Eng.*, vol. 9, no. 3, pp. 90–95, May 2007, doi: 10.1109/MCSE.2007.55.
[48] N. Sofroniew *et al.*, “napari: a multi-dimensional image viewer for Python,” *Zenodo*, May 2025, doi: 10.5281/zenodo.15465370.
[49] S. McKinley and M. Levine, “Cubic Spline Interpolation,” *Coll. Redw.*, 1998.
[50] J. Li, F. Xue, and T. Blu, “Fast and accurate three-dimensional point spread function computation for fluorescence microscopy,” *JOSA A*, vol. 34, no. 6, pp. 1029–1034, Jun. 2017, doi: 10.1364/JOSAA.34.001029.
[51] S. F. Gibson and F. Lanni, “Experimental test of an analytical model of aberration in an oil-immersion objective lens used in three-dimensional light microscopy,” *JOSA A*, vol. 9, no. 1, pp. 154–166, Jan. 1992, doi: 10.1364/JOSAA.9.000154.

[52] N. Otsu, “A Threshold Selection Method from Gray-Level Histograms,” *IEEE Trans. Syst. Man Cybern.*, vol. 9, no. 1, pp. 62–66, Jan. 1979, doi: 10.1109/TSMC.1979.4310076.
[53] F. Aguet, M. Jacob, and M. Unser, “Three-dimensional feature detection using optimal steerable filters,” in *IEEE International Conference on Image Processing 2005*, Sep. 2005, p. II–1158. doi: 10.1109/ICIP.2005.1530266.
[54] W. T. Freeman and E. H. Adelson, “The design and use of steerable filters,” *IEEE Trans. Pattern Anal. Mach. Intell.*, vol. 13, no. 9, pp. 891–906, 1991.
[55] H. Knutsson, “Representing local structure using tensors. Linkoping: Linkoping University,” *Comput. Vis. Lab.*, 1989.
[56] C. L. Luengo, L. J. van Vliet, B. Rieger, and M. van Ginkel, “DIPimage: a scientific image processing toolbox for Matlab Delft University of Technology.” 1999.
[57] L. J. van Vliet, “Grey-scale measurements in multi-dimensional digitized images,” PhD Thesis, Ph. D. Thesis of the Pattern Recognition Group, Delft University of …, 1993.
[58] P. W. Verbeek and L. J. van Vliet, “On the location error of curved edges in low-pass filtered 2-D and 3-D images,” *IEEE Trans. Pattern Anal. Mach. Intell.*, vol. 16, no. 7, pp. 726–733, Jul. 1994, doi: 10.1109/34.297954.
[59] P. W. Verbeek and J. Dijk, “The D-Dimensional Inverse Vector-Gradient Operator and Its Application for Scale-Free Image Enhancement,” in *Computer Analysis of Images and Patterns*, N. Petkov and M. A. Westenberg, Eds., Berlin, Heidelberg: Springer, 2003, pp. 738–745. doi: 10.1007/978-3-540-45179-2_90.

Appendix I

Here we describe a supplementary analysis of the main dataset where we include sign recovery for the principal curvatures. The full analysis presented here was performed in a similar manner as the absolute Gaussian curvature analysis described in *section 3*, unless specified otherwise. *Figure S1a* shows a logarithmic two-dimensional histogram of the Gaussian curvature and lamin B1 intensity of the filtered dataset, with the mean, median and upper 95th percentile intensities at all curvatures. *Figure S1b* shows the total intensity histogram of the filtered dataset and *figure S1c* shows the logarithmic total Gaussian curvature histogram of the filtered dataset. A total of 32.0% of the segmented voxels in this dataset represent a negative Gaussian curvature.

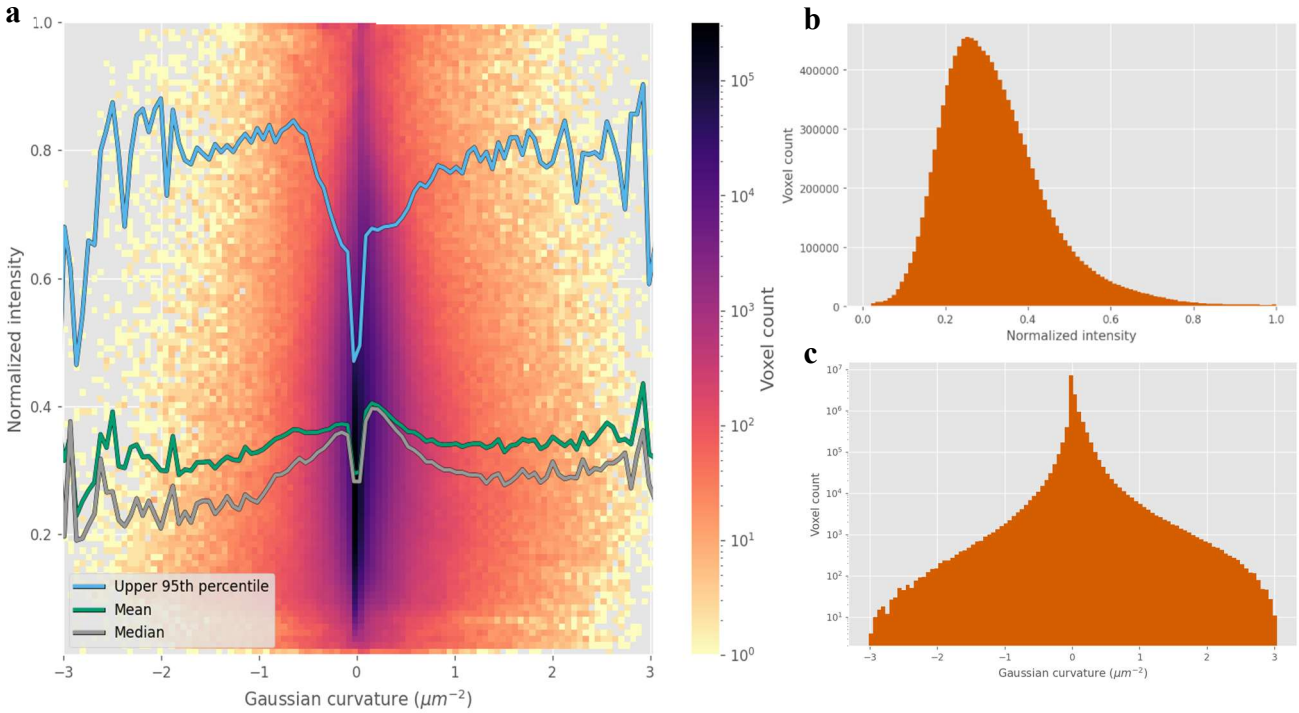

Figure S1. Gaussian curvature and lamin B1 intensity of the dataset, filtered with $|\kappa_{max}|$ = 1.769 µm^{-1}. N = 12 909 976 voxels. **a.** Two-dimensional histogram for Gaussian curvature and normalized lamin B1 intensity, with the mean, median and upper 95th percentile intensities for all curvatures. **b.** The total intensity histogram for the filtered dataset. **c.** The total Gaussian curvature histogram for the filtered dataset.

The lower Gaussian curvature limit of 0.15 µm^{-2} reduced the total dataset by 89.2%. The double Poisson function was fitted on the total intensity histogram of the restricted dataset as shown in *figure S2a*. The high-intensity occupancy for each curvature and the fitted probability model following *formula 1* are shown in *figure S2b*. The cut-off Gaussian curvature K_c was computed with the ratio E/a = 0.70 µm^{-1}, as described in *section 1.3*, and *formula 2,* resulting in K_c = 0.49 µm^{-2}. The majority of lamin B1 depletion occurs around the cut-off Gaussian curvature K_c, between Gaussian curvatures 0.2 µm^{-2} and 0.8 µm^{-2}. The upper and lower bound for the sigmoid probability function in *figure S2b* are 0.96 and 0.46, respectively. These bounds imply that the occupancy of the high-intensity population is 96% for the low-curvature regime and 46% for the high-curvature regime. Additionally, *figure S2c* shows the intensity histogram and fitted Poisson functions for several curvature ranges between 0.15 µm^{-2} and 0.90 µm^{-2}.

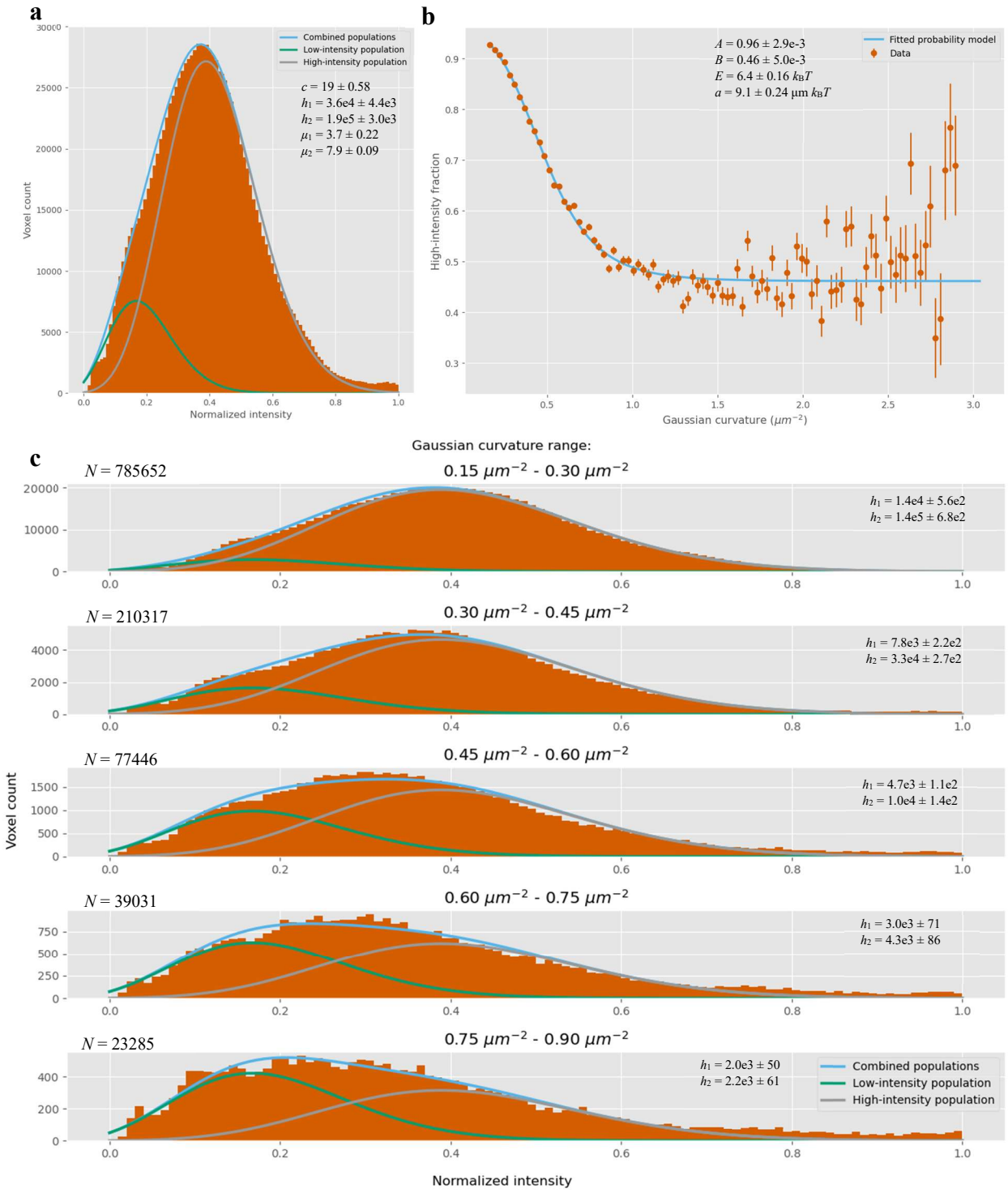

Figure S2. Intensity histograms and fitted probability model for the dataset, filtered with $|\kappa_{max}|$ = 1.769 μm^{-1} and restricted with a lower Gaussian curvature limit of 0.15 μm^{-2}. N = 1 168 418 voxels. **a.** Total intensity histogram with the fitted double Poisson function and component Poisson functions as described in *formula 13*. **b.** The occupancy of the high-intensity population, with standard deviations as described in *formula 15*, with the fitted probability model as described in *formula 1*. **c.** Intensity histograms for several curvature ranges with the fitted double Poisson function and component Poisson functions as described in *formula 13*. Total voxel count N is noted at each histogram.

Parameter	Prior studies	Main analysis	Supplementary analysis
E	4.7 – 5.1 k_BT	5.7 k_BT	6.4 k_BT
a	8.2 – 20 μm k_BT	8.3 μm k_BT	9.1 μm k_BT
K_c	0.05 – 0.40 μm^{-2}	0.48 μm^{-2}	0.49 μm^{-2}

Table S1. Comparison of several fitted parameters for the probability model described by *formula 1* between prior studies, the main analysis and the supplementary analysis with sign recovery.

All supplementary results closely resembled those found from the absolute Gaussian curvature as shown in *table S1*. The dataset was smaller as negative Gaussian curvatures are not used. Additionally, it is important to state again that the sign recovery was only moderately successful and these results do not represent reliable data as shown in *figure 19*. However, the analysis of Gaussian curvature with sign recovery still shows that the studied probability model holds for this case.

Appendix II

In addition to the main dataset described in *section 3*, the analysis was performed on supplementary dataset. This dataset has a larger voxel size of 0.090×0.090×0.299 µm and provided 12 FOVs with a total of 34 segmented nuclei. The voxel size is significantly larger than the Nyquist rate mentioned in *section 2.1*, which makes the analysis of the supplementary dataset less reliable. The supplementary dataset also did not contain DNA information, rendering sign recovery for the principal curvatures impossible. Hence, the analysis was performed only on the absolute Gaussian curvature. The full analysis was identical to the absolute Gaussian curvature analysis described in *section 3*, unless specified otherwise.

A number of parameters were re-evaluate for the supplementary dataset due to differences in acquisition settings, such as the increased voxel size. *Figure S3* shows that, although the robustness of σ_m seems to differ slightly, robust parameters for the supplementary dataset can be set identical to those for the main dataset as described in *section 3.1*. Thus, the parameter values are chosen to be d = 4 µm, σ_m = 0.9 µm, i_c = 0.25 of the maximum intensity of I_b and α = 0.9. Lastly, as the voxel size for this dataset is different, so is the lower limit for parameter σ_h. The minimum required value is 2.7 voxels [58], in this case 0.243 µm, which is still met by previously determined value σ_h = 0.420 µm.

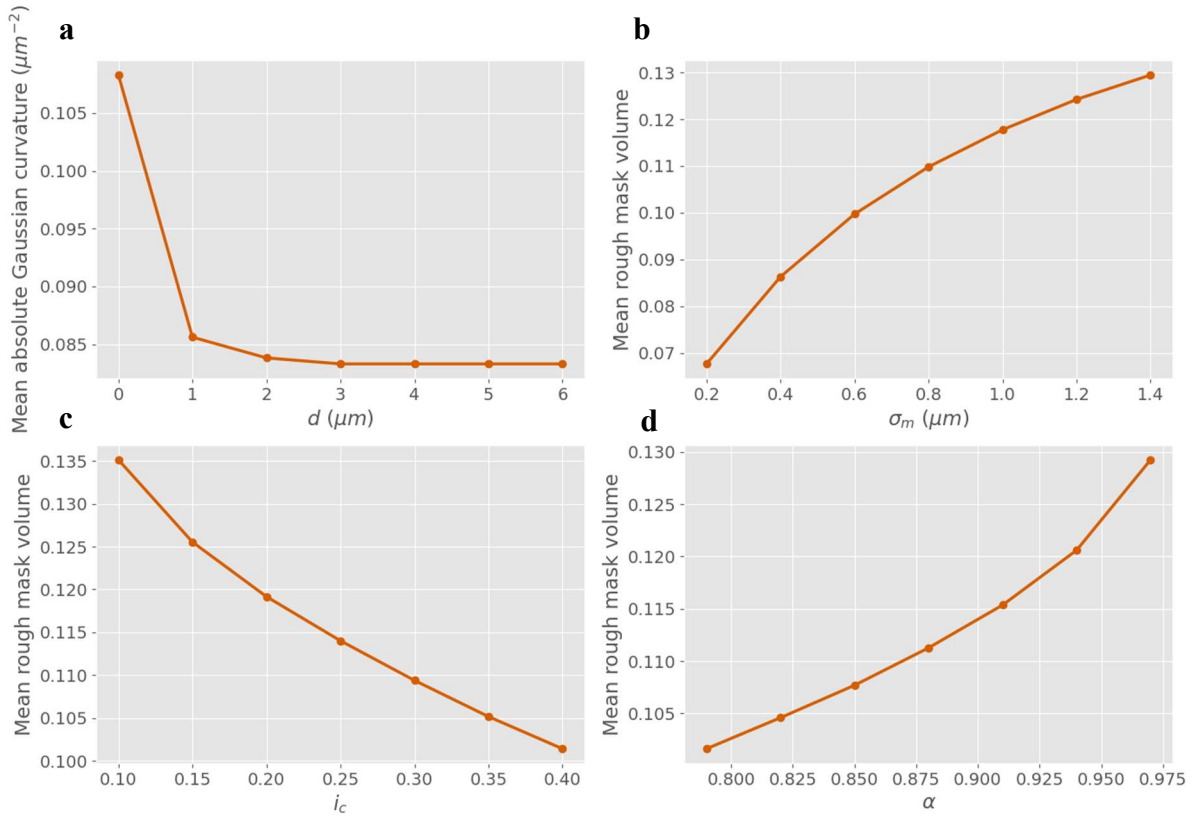

Figure S3. Robustness for labeling and segmentation parameters, N = 34 nuclei. **a.** The mean absolute Gaussian curvature within the fine segmentation of the nuclear lamina for different values of the parameter d. A robust value of d = 4 µm was chosen. **b-d.** The mean volume of the rough segmentation as a fraction of the total image volume for different values of segmentation parameters. **b.** A robust value of σ_m = 0.9 µm was chosen. **c.** A robust value of i_c = 0.25 was chosen. **d.** A robust value of α = 0.9 was chosen.

Filtering out all voxels with absolute principal curvatures exceeding 1.769 μm^{-1}, reduced the dataset by 1.3%. *Figure S4a* shows a logarithmic two-dimensional histogram of the absolute Gaussian curvature and lamin B1 intensity of the filtered dataset, with the mean, median and upper 95th percentile intensities at all curvatures. *Figure S4b* shows the total intensity histogram of the filtered dataset and *figure S4c* shows the logarithmic total absolute Gaussian curvature histogram of the filtered dataset.

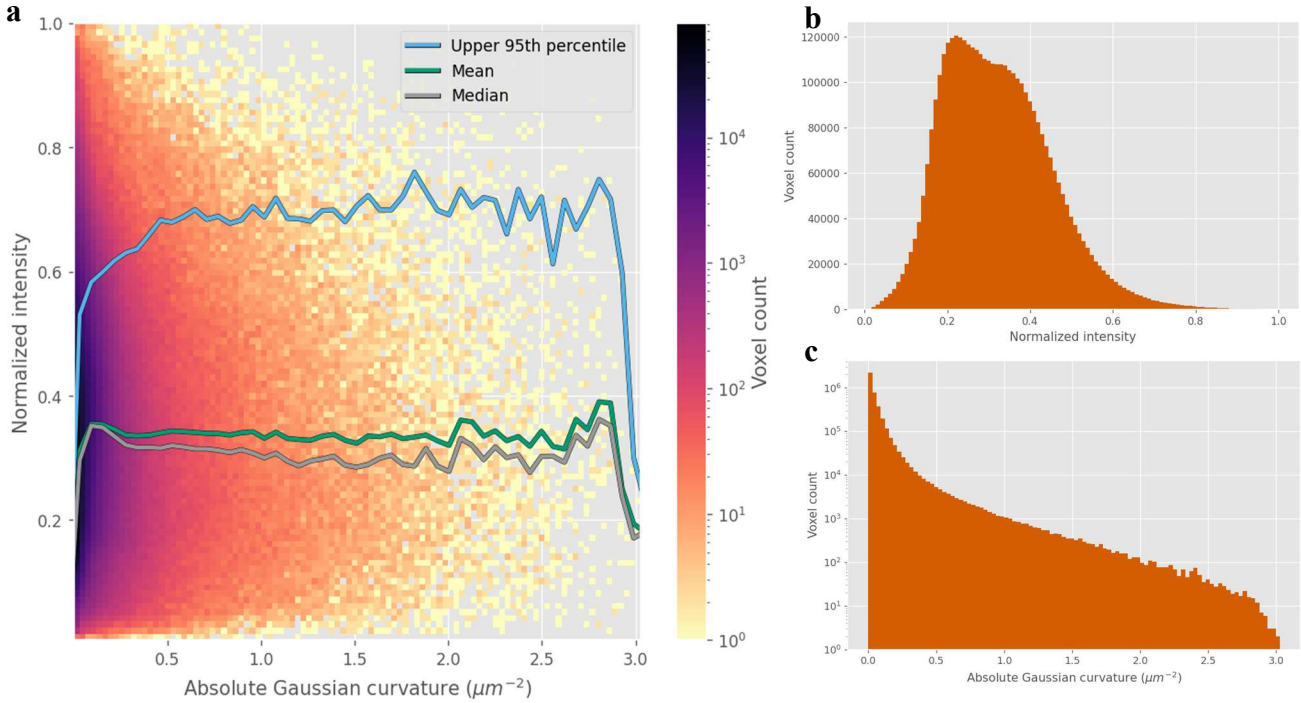

Figure S4. Absolute Gaussian curvature and lamin B1 intensity of the dataset, filtered with $|\kappa_{max}|$ = 1.769 μm^{-1}. N = 12 909 976 voxels. **a.** Two-dimensional histogram for absolute Gaussian curvature and normalized lamin B1 intensity, with the mean, median and upper 95th percentile intensities for all curvatures. **b.** The total intensity histogram for the filtered dataset. **c.** The total absolute Gaussian curvature histogram for the filtered dataset.

The lower absolute Gaussian curvature limit of 0.15 μm^{-2} reduced the total dataset by 84.8%. The double Poisson function was fitted on the total intensity histogram of the restricted dataset as shown in *figure S5a*. The high-intensity occupancy for each curvature and the fitted probability model following *formula 1* are shown in *figure S5b*. The cut-off Gaussian curvature K_c was computed with the ratio E/a = 0.41 μm^{-1}, as described in *section 1.3* and by *formula 2,* resulting in K_c = 0.17 μm^{-2}. The majority of lamin B1 depletion occurs around the cut-off Gaussian curvature K_c, between absolute Gaussian curvatures of 0.1 μm^{-2} and 0.3 μm^{-2}. The upper and lower bound for the sigmoid probability function in *figure S5b* are 1.00 and 0.53, respectively. These bounds imply that the occupancy of the high-intensity population is 100% for the low-curvature regime and 53% for the high-curvature regime. *Figure S5c* shows the intensity histogram and fitted Poisson functions for several curvature ranges between 0.15 μm^{-2} and 0.90 μm^{-2}.

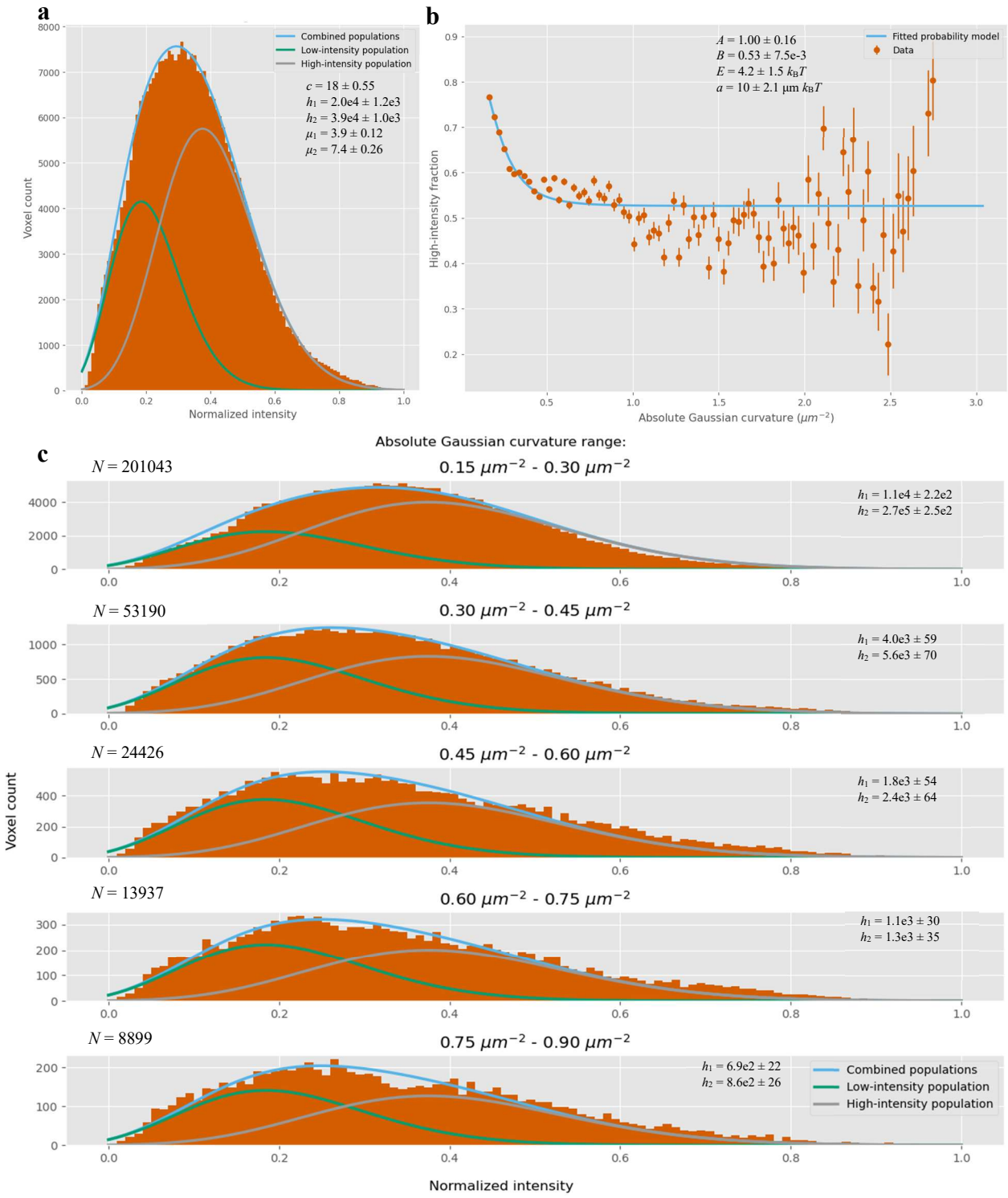

Figure S5. Intensity histograms and fitted probability model for the dataset, filtered with $|\kappa_{max}|$ = 1.769 μm^{-1} and restricted with a lower absolute Gaussian curvature limit of 0.15 μm^{-2}. N = 558 364 voxels. **a.** Total intensity histogram with the fitted double Poisson function and component Poisson functions as described in *formula 13*. **b.** The occupancy of the high-intensity population, with standard deviations as described in *formula 15*, with the fitted probability model as described in *formula 1*. **c.** Intensity histograms for several curvature ranges with the fitted double Poisson function and component Poisson functions as described in *formula 13*. Total voxel count N is noted at each histogram.

Parameter	Prior studies	Main dataset	Supplementary dataset
E	4.7 – 5.1 k_BT	5.7 k_BT	4.2 k_BT
a	8.2 – 20 μm k_BT	8.3 μm k_BT	10 μm k_BT
K_c	0.05 – 0.40 μm^{-2}	0.48 μm^{-2}	0.17 μm^{-2}

Table S2. Comparison of fitted parameters for the probability model described by *formula 1* between prior studies, the main dataset and the supplementary dataset.

The results from the supplementary dataset corresponded to the findings from other studies but differed from the main results in *section 3.3* as shown in *table S2* [18], [19]. Unfortunately, a large part of the depletion range was not considered as a lower absolute Gaussian curvature limit of 0.15 μm^{-2} was set, implying that valuable information was lost with this restriction. It is also important to note that the sample size of this dataset is smaller, with only 34 nuclei instead of 76 nuclei and only half the number of segmented voxels. A second restraint for this dataset is the larger voxel size, falling outside the near-optimal range around the Nyquist rate as described in *section 2.1*. This might have caused the formation of curvature artifacts, as the intensity signal is discretized around the edges of the nuclear lamina. However, the analysis of this supplementary dataset still shows that the global probability model holds for different datasets and acquisition settings.